American Mineralogist, Volume 103, pages 91–108, 2018

New insights into the metallogeny of MVT Zn-Pb deposits: A case study from the Nayongzhi in South China, using field data, fluid compositions, and in situ S-Pb isotopes

Jia-Xi Zhou[1,2,*], Xuan-Ce Wang[2], Simon A. Wilde[2], Kai Luo[1,3], Zhi-Long Huang[1], Tao Wu[4], and Zhong-Guo Jin[1]

[1]State Key Laboratory of Ore Deposit Geochemistry, Institute of Geochemistry, Chinese Academy Sciences, Guiyang 550081, China
[2]The Institute for Geoscience Research, Department of Applied Geology, Curtin University, GPO Box U1987, Perth, West Australia 6845, Australia
[3]University of Chinese Academy Sciences, Beijing 100049, China
[4]School of Earth Sciences, Zhejiang University, Hangzhou 310027, China

Abstract

The newly discovered Nayongzhi Zn-Pb deposit (>20 Mt ores at 1.11–15.65 wt% Zn and 0.59–0.97 wt% Pb) in NW Guizhou province, South China, is hosted by late Ediacaran and early Cambrian carbonate rocks. The ore body is structurally controlled by a kilometer-scale reverse fault-anticline system and occurs as stratiform, lentiform, or steeply dipping vein structures. Its geological feature is comparable to that of the Mississippi Valley-type (MVT) Zn-Pb deposits. $\delta^{34}S$ values (+11.8 to +33.0‰) of sulfide minerals determined by NanoSIMS have a larger range than those determined by conventional bulk analysis ($\delta^{34}S$ = +18.12 to +24.79‰). This suggests that S isotopes determined by in situ analysis can reflect the nature of fractionation involved in mineralization. Furthermore, cores of sulfide crystals have higher $\delta^{34}S$ values (+26.1 to +33.0‰) than their rims (+11.8 to +24.5‰). This implies a mixture of multiple S reservoirs or a Rayleigh fractionation of S isotopes occurred during ore formation process. Additionally, both S isotopic compositions determined by in situ and bulk analyses reflect the enrichment of ^{34}S in hydrothermal fluid ($\delta^{34}S_{fluid}$ > +11.8‰), a typical characteristic of marine sulfate-derived S. Such S isotopic signatures also show that thermochemical sulfate reduction (TSR) is the dominant mechanism for the incorporation of S^{2-} from SO_4^{2-}. Pb isotopic ratios of galena obtained by femtosecond LA-MC-ICPMS plot in the field that overlaps with the Pb evolution curve of upper crust contributed to the orogeny and the field of modern lower crust, and can be compared to the Proterozoic metamorphic rocks. The means that the majority of Pb metal is sourced from the basement rocks. Although $\delta^{13}C$ values (–4.1 to +0.5‰) of calcite separates and corresponding fluids are similar to both fresh limestone (–1.7 to +1.3‰) and typical marine carbonate rocks, the $\delta^{18}O$ values (+12.4 to +14.1‰) are significantly lower than both limestone (+24.1 to +25.5‰) and marine carbonate rocks. Such C-O isotopic characteristics suggest that the source of C is ore-hosting carbonate rocks, whereas O has a mixed source of metamorphic fluids and carbonate rocks resulting from water/rock (W/R) interaction. This study demonstrates that (1) fluid mixing caused rapid sulfide precipitation, resulting in significant fractionation of S isotopes; and (2) both the W/R interaction and CO_2 degassing controlled local carbonate cyclic process of dissolution → re-crystallization, which provided metastable physical and chemical conditions for giant sulfide mineralization. These two processes are crucial in forming MVT deposits.

Keywords: In situ S-Pb isotopes, fluid mixing, buffer of carbonate, MVT deposits, South China

Introduction

Zn-Pb deposits hosted by carbonate or siliciclastic rocks contain the world's greatest Zn and Pb resources and predominate the world production of these metals (Leach et al. 2005). They are known as sediment-hosted types of ore deposit and generally have no direct genetic association with igneous activity (Leach et al. 2010). Carbonate-hosted Zn-Pb deposits, one of the two major subtypes of sediment-hosted Zn-Pb deposits, occur in platform carbonate sequences and are commonly named as the Mississippi Valley-type (MVT) deposits (Leach et al. 2010). Extensive research on the MVT deposits has dedicated greatly to our understanding of fluid flow and metal transport in sedimentary basin (Heijlen et al. 2003; Leach et al. 2005; Wilkinson et al. 2009). However, as the MVT deposits are the products of various ore formation processes in a wide range of geologic and tectonic environments (Gustafson and Williams 1981; Wilkinson et al. 2009; Leach et al. 2010), so their ore genesis is still controversial, and the chemical and isotopic evolution of hydrothermal fluids also needs to be careful constrained.

In China, carbonate-hosted Zn-Pb deposits are widely distributed in the platform carbonate sequences surrounding the Yangtze

* E-mail: zhoujiaxi@vip.gyig.ac.cn

0003-004X/18/0001–091$05.00/DOI: http://dx.doi.org/10.2138/am-2018-6238

Craton (Zaw et al. 2007; Wang et al. 2014; Hu et al. 2017). For example, more than 400 Zn-Pb deposits in the western Yangtze Craton form the Sichuan-Yunnan-Guizhou (SYG) Pb-Zn metallogenic province (Figs. 1a–1b) with more than 200 Mt ores grading 10–15 wt% Zn + Pb (Zhou et al. 2013a, 2014a). Such a province is an important part of the giant South China low-temperature metallogenic domain (Hu et al. 2017), accounting for 27% of total Zn + Pb resources in China (Zhang et al. 2015). Extensive investigation on the origin of the Zn-Pb deposits in the SYG province has been carried out in the past two decades, although they belong to epigenetic type is widely recognized, there is still a struggle of ore genesis, such as MVT (Zheng and Wang 1991; Zhou et al. 2001; Wang et al. 2014; Zhang et al. 2015; Zhu et al. 2017), distal magmatic-hydrothermal type (Xie 1963; Huang et al. 2010; Bai et al. 2013; Xu et al. 2014) or unique SYG-type (Zhou et al. 2013b, 2014b; Li et al. 2015, 2016; Zhu et al. 2016).

Microbeam analytical techniques have potential to provide key in situ elemental and isotopic information to constrain the sources of mineralizing elements and associated fluids, as well as the metallogenic environments of the hydrothermal system (Liu et al. 2008; Barker et al. 2009; Steinhoefel et al. 2009; Ye et al. 2011; Zhang et al. 2014; Yuan et al. 2015; Jin et al. 2016). Such information is crucial for understanding the metallogeny of hydrothermal deposits. Secondary ion mass spectroscopy (SIMS) and laser ablation-multicollector-inductively coupled plasma mass spectrometry (LA-MC-ICPMS) are techniques that can efficiently determine microscale isotopic compositions of sulfide minerals in hydrothermal deposits (Peevler et al. 2003; Ikehata et al. 2008; Chen et al. 2014; Bao et al. 2016).

Here we use the newly discovered Nayongzhi MVT Zn-Pb deposit that is situated in the southeastern part of the SYG province as a case, and we report a set of NanoSIMS in situ S, femtosecond LA-MC-ICPMS in situ Pb, and conventional whole-rock C and O isotopic data. Through integrating the newly obtained data and detailed ore deposit geology, this study aims to reveal the origin and evolution of hydrothermal fluids, and then to propose a new genetic model for the Nayongzhi deposit. The outcomes are crucial for understanding the formation and exploration of MVT deposits in general.

Geological setting

General geology of the western Yangtze Craton

The Yangtze Craton constitutes a significant part of the South China Block and is bounded by the Cathysia Block to the southeast, the Qinling-Dabie Orogenic Belt to the north, the Songpan-Ganzê Orogenic Belt to the northwest, and the Sanjiang Orogenic Belt

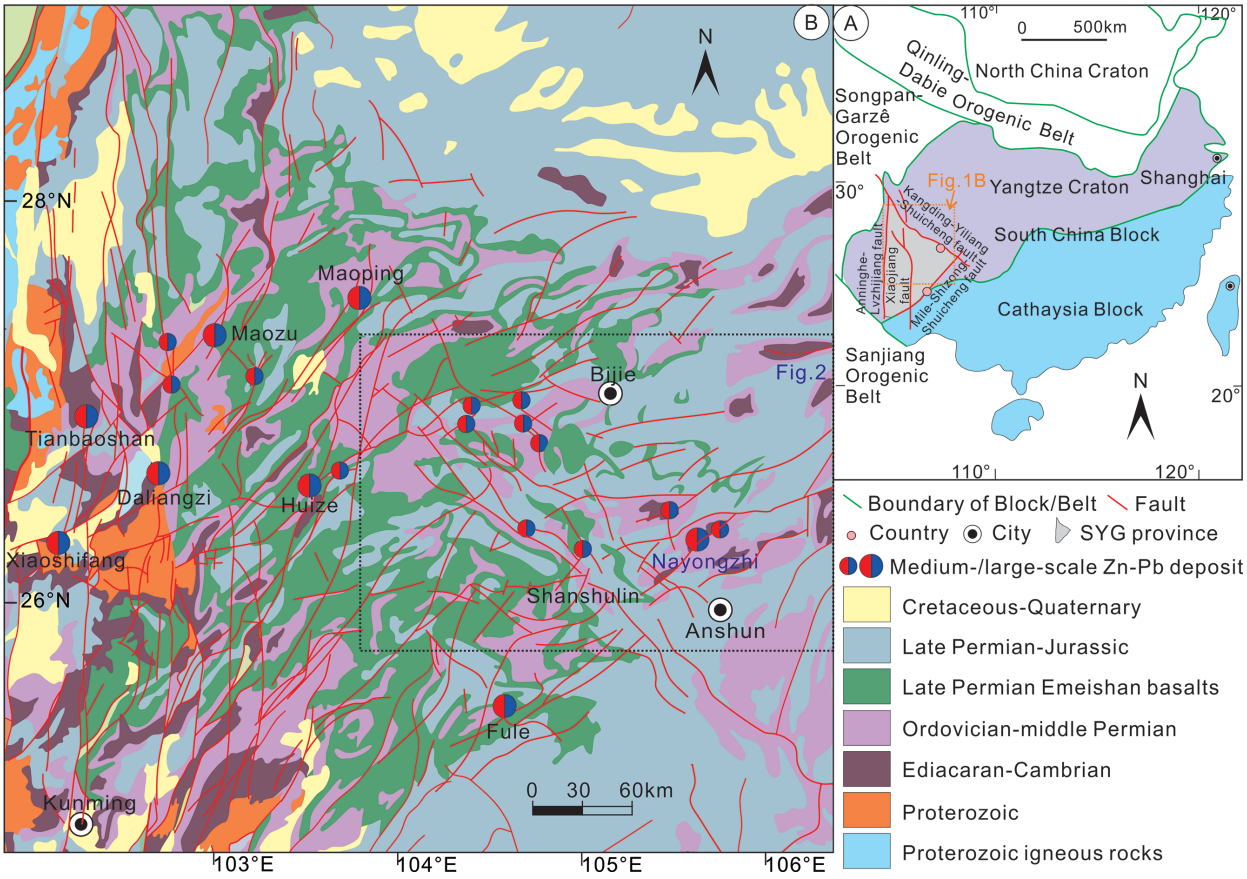

Figure 1. (**a**) Regional geological setting of South China, highlighting the general study area. (**b**) Geological sketch map of the Sichuan-Yunnan-Guizhou (SYG) Pb-Zn metallogenic province (modified from Liu and Lin 1999 and Yan DP unpublished map), which shows the distribution of Zn-Pb deposit, strata, fault, and Emeishan basalts. (Color online.)

to the southwest (Fig. 1a). The basement of the western Yangtze Craton consists of late Paleoproterozoic to early Neoproterozoic weakly metamorphic rocks, which were intruded by widespread late Neoproterozoic igneous rocks (Qiu et al. 2000; Zhou et al. 2002, 2014c; Gao et al. 2011). The sedimentary succession of the western Yangtze Craton is composed mainly of Cambrian to Triassic marine and Jurassic to Cenozoic continental sedimentary rocks (Yan et al. 2003; Zhou et al. 2013a; Hu et al. 2017). Sulfate-bearing evaporites are common in the Cambrian to Triassic marine sedimentary strata, which are an important S source for the sediment-hosted hydrothermal deposits in the western Yangtze Craton (Bai et al. 2013; Zhou et al. 2014a; Chen et al. 2015). Faults in the western Yangtze Craton are well developed and have undergone multi-stage activities (namely Hercynian, Indosinian, and Yanshanian orogenic events, and even Himalayan Orogeny), which primarily controlled the sedimentation, magmatism, and mineralization (Liu and Lin 1999), such as the regional NW-trending Yiliang-Shuicheng and NS-trending Xiaojiang faults (Figs. 1, 2, and 3).

A significant feature of the western Yangtze Craton is the occurrence of Emeishan Large Igneous Province (ELIP) and its flood basalts (ca. 260 Ma) with an area of more than 250 000 km^2 (Zhou et al. 2002; Jian et al. 2009). After eruption of late Permian Emeishan basalts, the western Yangtze Craton collided with the adjacent blocks (for example, Yidun Arc), resulting in the closure of the Paleo-Tethys ocean (Reid et al. 2007; Hu and Zhou 2012; Zhou et al. 2013a; Qiu et al. 2016; Hu et al. 2017). This event is named as the Indosinian Orogeny (257–205 Ma) (Carter et al. 2001). After then, there is the Yanshanian Orogeny that occurred during Jurassic-Cretaceous (205–135 Ma) time (Wong 1927; Reid et al. 2007). These two orogenic events resulted in faulting and folding that significantly controlled the distribution of carbonate-hosted Zn-Pb deposits in the western Yangtze Craton (Liu and Lin 1999; Huang et al. 2010; Zhou et al. 2014b; Zhang et al. 2015).

Another significant feature of the western Yangtze Craton is the occurrence of the SYG Zn-Pb mineralization province and its 408 Zn-Pb deposits with an area of more than 170 000 km^2 (Liu and Lin 1999; Zhou et al. 2014a; Wei et al. 2015; Hu et al. 2017). All the Zn-Pb deposits host in the late Ediacaran to middle Permian carbonate rocks and are spatially associated with the late Permian Emeishan basalts (Fig. 1b). Calcite/fluorite Sm-Nd, sphalerite/pyrite Rb-Sr, and bitumen Re-Os isotope geochronology studies suggest that these carbonate-hosted Zn-Pb deposits formed between 226 and 165 Ma (Li et al. 2007; Lin et al. 2010; Mao et al. 2012; Zhou et al. 2013a, 2013b, 2015; Zhang et al. 2015; Hu et al. 2017). This indicates that the Zn-Pb mineralization in the SYG province occurred during late Triassic-middle Jurassic, and related to the Indosinian and Yanshanian two orogenic events.

Regional geology of the NW Guizhou district

The newly discovered Nayongzhi carbonate-hosted Zn-Pb deposit is located in NW Guizhou province (Figs. 1b, 2, and 3). In the NW Guizhou district, the basement rocks of the western Yangtze Craton are not exposed (Figs. 2–3). The cover sequences including late Ediacaran to Triassic marine and Jurassic continental sedimentary rocks, as well as late Permian Emeishan continental flood basalts. The late Ediacaran strata consist mainly of limestone and dolostone. The Cambrian strata are composed dominantly of siltstone, claystone, limestone, argillaceous dolostone, and dolomitic sandstone. These sedimentary rocks of late Ediacaran and Cambrian are unconformably overlain by Devonian strata that consist predominantly of sandstone, siltstone, shale, limestone, and dolostone. The Devonian sedimentary rocks are normally overlain by Carboniferous strata, which are

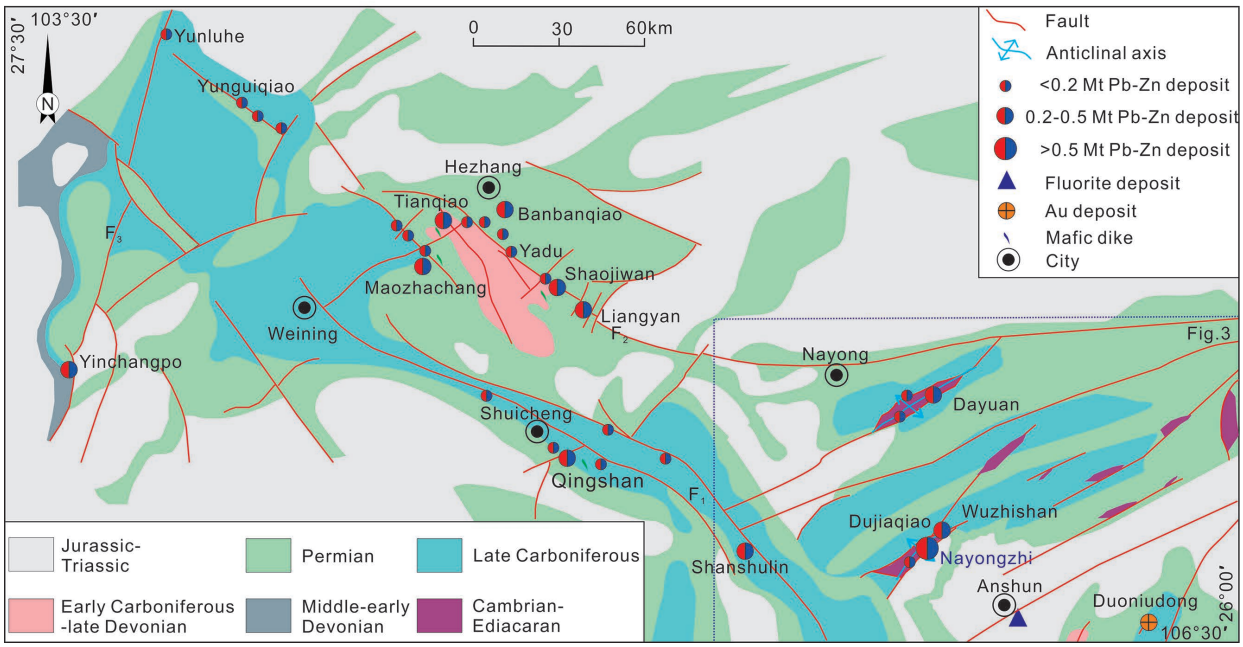

FIGURE 2. Geological sketch map of the NW Guizhou Zn-Pb metallogenic district (modified from Zhou et al. 2013a), which shows the distribution of Zn-Pb deposit, strata, fault, and mafic dikes. (Color online.)

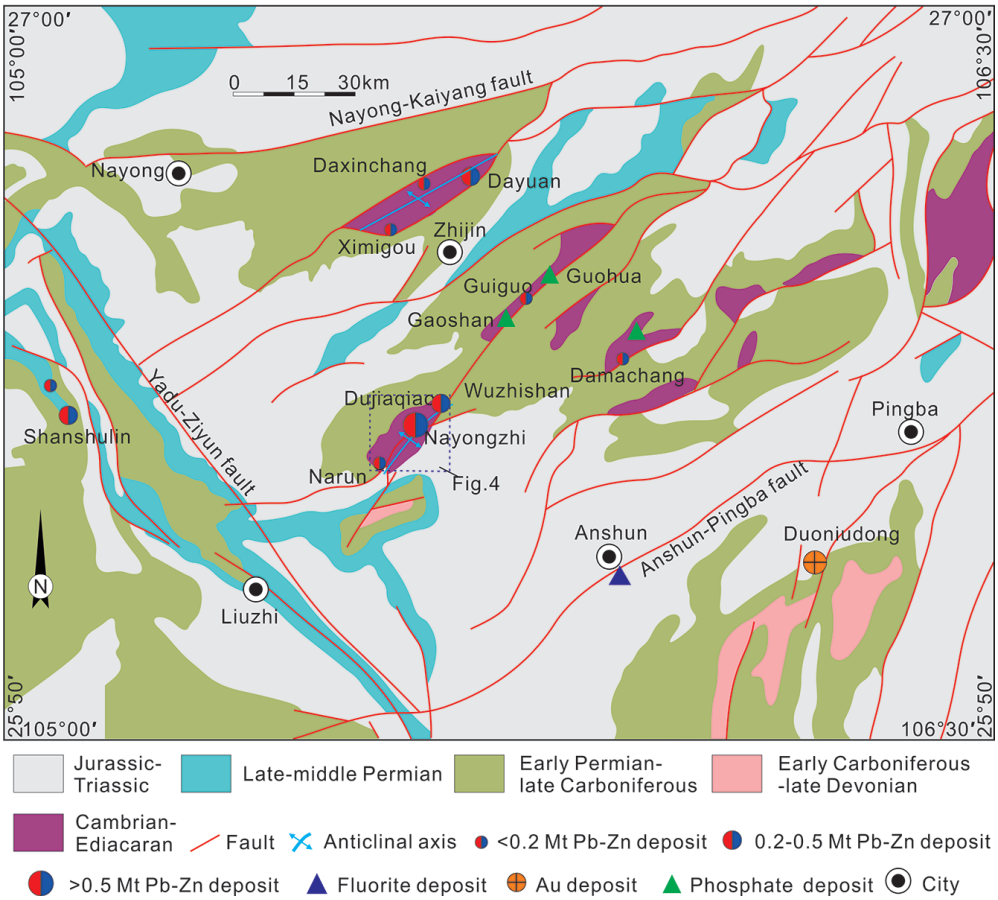

FIGURE 3. Geological sketch map of the southeastern part of the NW Guizhou district (modified from Chen et al. 2015a), which displays the fault, strata, ore-controlling structure, and Zn-Pb, Au, phosphate, and fluorite deposits. (Color online.)

composed mainly of shale, limestone, and dolostone. The early-middle Permian sequence consists dominantly of sandstone, shale, coal layers, and limestone, all of which are unconformably overlain by the late Permian Emeishan flood basalts. The basalts, in turn, are overlain by sandstone, siltstone, and coal measures of the late Permian strata. The Triassic strata consist mainly of siltstone, sandstone, dolostone, and limestone, and the Jurassic strata are dominated by sandstone. The Zn-Pb sulfide ores are hosted by the late Ediacaran to middle Permian carbonate rocks and parts of them have a spatial association with late Permian basalts (Tu 1984; Jin 2008; Zhou et al. 2013a; Li et al. 2015; Figs. 1b, 2, and 3).

NW- and NE-striking faults and folds are well developed in the NW Guizhou district, for example, the NW-trending Yadu-Ziyun fault (Figs. 1b, 2, and 3), the NE-trending Nayong-Kaiyang and Anshun-Pingba faults, and the NE-trending Dayuan and Wuzhishan anticlines (Figs. 2–3). Among these structures, the Yadu-Ziyun regional fault controlled the sedimentation and low-temperature mineralization (Zn-Pb, Au, and fluorite deposits) in the studied region (Figs. 2–3). Mafic dikes (diabase), related to the ELIP (Jin 2008), also occur in this district and spatially associate with parts of Zn-Pb deposits (Fig. 2).

More than 100 carbonate-hosted Zn-Pb deposits have been found in the NW Guizhou district, such as the Tianqiao and Shanshulin deposits (Figs. 1, 2, and 3; Jin 2008; Zhou et al. 2013a, 2014b). The Nayongzhi Zn-Pb deposit, discovered in 2011, occurs in the southeastern part of the NW Guizhou district (Figs. 2–3) and is hosted by limestone and dolostone of late Ediacaran Dengying Formation and early Cambrian Qingxudong Formation (Figs. 4–6). This deposit is the largest and only large-scale (>0.5 Mt Zn + Pb metal reserve) carbonate-hosted Zn-Pb deposit in the Guizhou part of the SYG province (Jin et al. 2016), containing Zn + Pb metal reserve of more than 1.5 Mt with ore grades of 1.11–15.65 wt% Zn and 0.59–0.97 wt% Pb.

GEOLOGY OF THE NAYONGZHI ZN-PB DEPOSIT

Stratigraphy and lithology

The Nayongzhi deposit is situated in the central part of the Wuzhishan anticline (Figs. 2–4). In the Wuzhishan anticline area, the exposed strata are late Ediacaran, Cambrian, early Carboniferous, early Permian, and early Triassic (Figs. 4–5). The late Ediacaran Dengying Formation consists mainly of limestone and dolostone, which are normally overlain by the early Cambrian Jindingshan Formation that is composed dominantly of siltstone and shale. Followed the Jindingshan Formation is the early Cambrian Qingxudong Formation, which is mainly

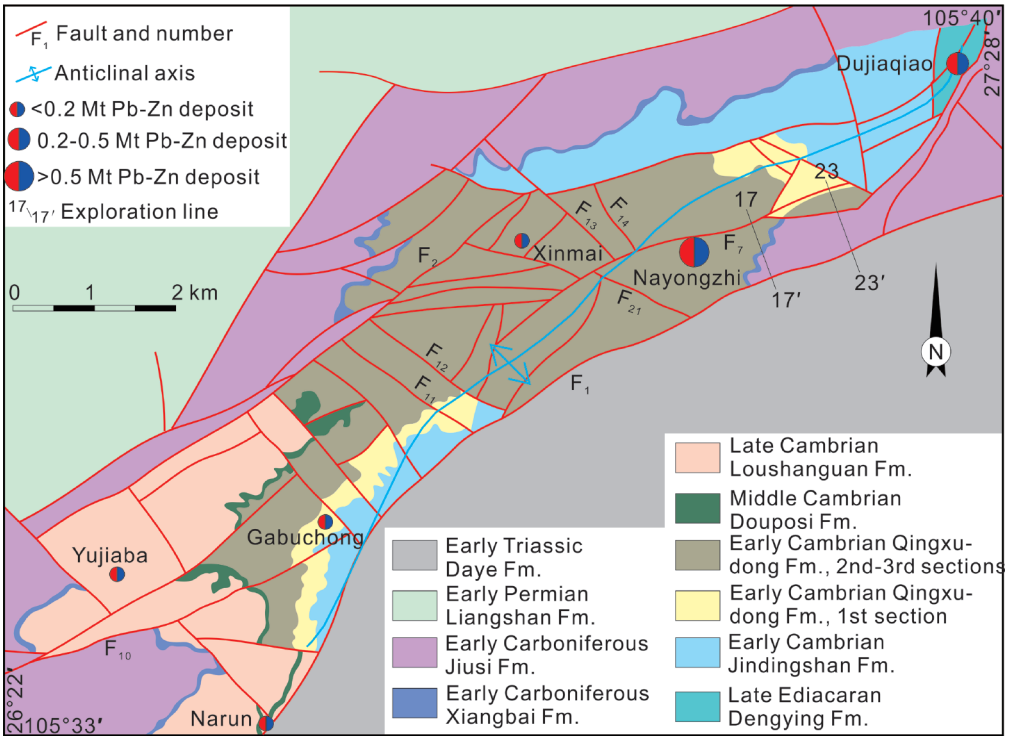

FIGURE 4. Geological sketch map of the Wuzhishan anticline area (modified from Peng et al. 2016), which reveals the ore-controlling structure, strata, and Zn-Pb deposit. (Color online.)

made up of limestone and dolostone. The middle Cambrian Douposi Formation is composed predominantly of dolostone and sandstone, and the late Cambrian Loushanguan Formation is dominated by limestone and dolostone. The early Carboniferous strata comprise the Xiangbai and Jiusi formations, which consist mainly of limestone and siltstone, and shale and limestone, respectively. The early Permian Liangshan Formation consists dominantly of shale and sandstone, and the early Triassic Daye Formation is mainly made up of limestone. In the Nayongzhi mining area, the exposed strata are Qingxudong Formation (Fig. 4) that can be subdivided into three sections based on the lithological feature, of which the first and second sections have six and two lithological layers, respectively (Fig. 5). Zn-Pb ores host in the limestone and dolostone of the Dengying Formation, and the first section and the first layer of the second section of the Qingxudong Formation (Figs. 5, 6a, and 6b).

Tectonics

In the Wuzhishan anticline area, the tectonics are well developed and strictly control the distribution of Zn-Pb deposits (Figs. 3–4). The Wuzhishan anticline, a NE-trending asymmetric anticline, is 16 km long and 4 km wide with an axis trending angle of 45° (Fig. 4). The Narun fault (F_1 in Fig. 4), a normal structure, strikes NE and dips at SE. This fault intersects the Yadu-Ziyun regional fault to the southwest (Fig. 3). The Dujiaqiao fault (F_2 in Fig. 4) is a reverse fault that strikes 30° and dips at SE with a dipping angle of 60–70°. Another important fault, F_7 reverse fault (Fig. 4), trends north with a dipping angle of 51–75°. Studies suggest that the Wuzhishan anticline, and NE- and NW-trending faults were active during the Yanshanian Orogeny (Chen et al. 2015a). In the Nayongzhi ore district, sulfide ore is structurally controlled by a reverse fault-anticline system, namely the F_7 reverse fault and Wuzhishan anticline (Figs. 4, 6a, and 6b).

Ore body

In the Nayongzhi ore district, one steeply dipping veined and 20 stratiform or lentiform ore bodies have been found in total until 2015 (Peng et al. 2016). The steeply dipping veined ore body occurs along the F_7 reverse fault zone (Figs. 6a and 7e), which is 20–50 m long, 0.5–3 m wide, and 200 m thick. This ore body contains high ore grade of Zn (>10 wt%), with less abundant Pb. The stratiform or lentiform ore bodies (Figs. 6a, 6b, and 7a) can be combined into three groups (I, II, and III) based on the lithological character of their ore-bearing layers (Figs. 5, 6a, and 6b). Ore bodies in these three groups are similar, of which the Group II is the largest and occurs in the fifth layer of the first section of the Qingxudong Formation (Figs. 5, 6a, and 6b). Here we take the Group II as an example to introduce the geology of ore body. Sulfide ore in this group is hosted by limestone and dolostone, with argillaceous limestone and dolostone as wall rocks. The ore bodies are stratiform or lentiform and have the same orientation as the ore-hosting rocks, namely strike NE and dip SE with a dipping angle of 8–20°. The main ore body in the Group II is 2725 m long, 250–775 m wide, and 1–29.6 m thick, containing 0.5–36.63 wt% Zn (average 4.03 wt%) and 0.04–4.05 wt% Pb (average 0.45 wt%). This ore body contains Zn + Pb metal reserve of more than 0.5 Mt and is the largest one in the Nayongzhi deposit.

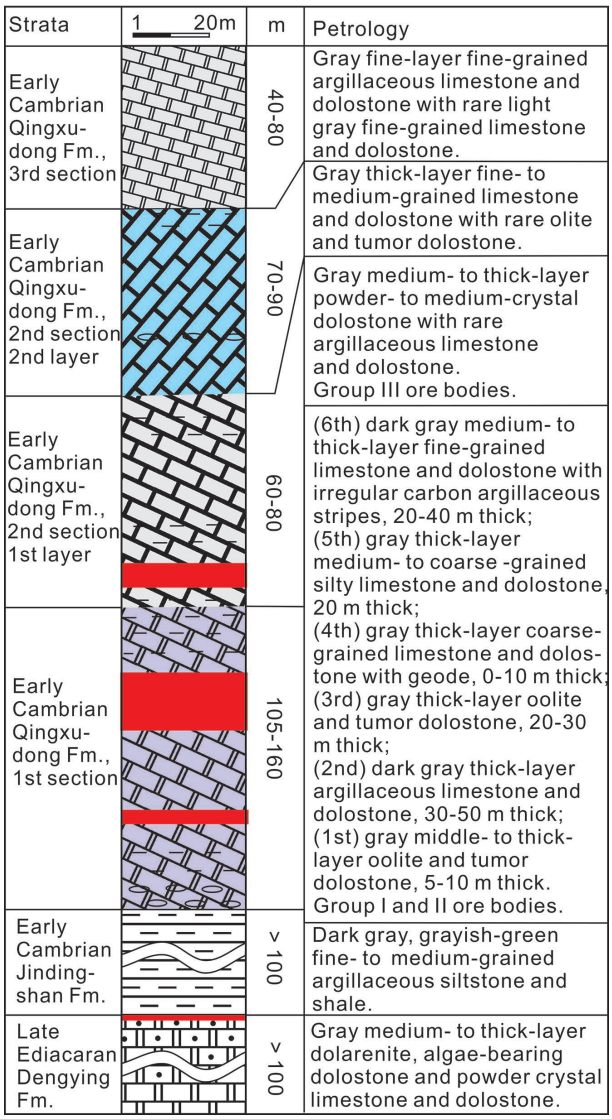

FIGURE 5. A generalized stratigraphic map of the Nayongzhi mining area, which shows the lithology of ore-hosting strata and location of Zn-Pb ore body. (Color online.)

Texture and structure of sulfide ores

Sulfide ore in the Nayongzhi deposit consists mainly of sphalerite, secondary galena, and pyrite, with calcite or dolomite as primary gangue minerals, and rare quartz or barite as local associated minerals (Figs. 7–10).

Sulfide ore in veined, stratiform or lentiform ore bodies occurs as either veined (Figs. 7b, 7d, 7g, 7j–7k, 7m, 7o, 9h, 9j, and 9l–9p), massive (Figs. 7c, 7k, 7n, 8d–8f, and 8i), or disseminated (Figs. 7h, 8a–8c, 8g, and 8l). Their general feature is as follows: (1) veined ore: sulfide minerals (sphalerite, galena, and pyrite) occur as veinlet or stockwork, and fill into fracture or cement carbonate solution collapse breccia (such as Figs. 7b, 7d, and 7g); (2) massive ore: sulfide minerals form massive aggregation in wall rocks (for example, Figs. 7c and 8d–8e); and (3) disseminated ore: sulfide minerals present as speckle aggregation that densely or sparsely distributes in wall rocks (e.g., Figs. 7h, 8a–8c, and 8g). Syn- or post-ore gangue minerals occur as crumb or veined aggregation that fills into fracture or cements carbonate breccia (such as Figs. 7b–7c, 7f, and 7h).

Sulfide minerals have granular, fragmented, or replacement textures (Figs. 9–10), which have general features as follows.

(1) Granular texture. Sphalerite presents as fine to coarse (0.01–10 mm) granular crystal that coexists with pyrite (Figs. 9c, 9f–9h, 10c–10e, and 10h–10j), galena (Figs. 9d, 9f–9g, 9j–9k, 9n–9o, 10b, 10g–10h, and 10k–10n), quartz (Fig. 9d), or calcite/dolomite (Figs. 9a, 9d, 9j–9k, 9m–9o, 10b, 10d, 10f, 10g–10i, and 10l–10p) and is enclosed by pyrite (Fig. 9b), galena (Figs. 9o and 10a), or calcite/dolomite (Figs. 9a–9c, 9e–9f, 10c, 10g–10j, 10l, and 10n–10o). Galena occurs as fine to medium (0.05–0.6 mm) granular crystal, coexisting with sphalerite (Figs. 9d, 9f–9g, 9j–9k, 9n–9o, 10b–10c, 10g–10h, and 10l–10n) and is enclosed by calcite/dolomite (Figs. 9f, 9k, 10a, 10g–10h, 10k–10l, and 10n), sphalerite (Figs. 10l and 10o), or pyrite (Fig. 10i). Pyrite occurs as fine (0.001–0.2 mm) granular crystal, coexisting with sphalerite (Figs. 9a–9c, 9f–9h, 10c–10f, and 10h–10j) and is enclosed by calcite/dolomite (Figs. 9c and 10j), galena (Fig. 10a), or sphalerite (Fig. 10p). Diagenetic pyrite is fine-grained and distributes in wall rocks (Fig. 8k) or is cemented by quartz (Fig. 9l).

(2) Fragmented texture. Fragmented sphalerite is enclosed by pyrite (Fig. 10d) or calcite/dolomite (Fig. 10j) and is filled by galena (Fig. 10k) or calcite/dolomite (Fig. 10p).

(3) Replacement texture. Sphalerite is replaced by galena (Fig. 9h) or replaces pyrite (Figs. 9m and 10f).

Mineral paragenesis

The Nayongzhi carbonate-hosted Zn-Pb deposit has experienced diagenetic, hydrothermal, and oxidized episodes (Appendix[1] Table 1), of which the hydrothermal period can be further subdivided into sulfide + (quartz + calcite/dolomite) and quartz + calcite/dolomite + (barite) stages (Figs. 7–10). There are two principal types of sulfide ore formed during the sulfide stage: sphalerite-dominated + pyrite + galena + quartz + calcite/dolomite, and sphalerite- and galena-dominated + pyrite + quartz + calcite/dolomite. The spatial distribution of sulfide ore (Fig. 7) shows the formation sequence is from sphalerite-dominated massive (Figs. 8d and 8i) or dense disseminated ore (Figs. 8a–8c and 8l), and sphalerite- and galena-dominated massive (Figs. 8e–8f) or sparely disseminated ore (Figs. 8g), to metasomatic, filled or cemented ore vein (Figs. 8h, 8j, and 8l–8p). Therefore, sulfide minerals have two generations (Appendix[1] A).

Wall rock alteration

Wall rock alteration includes dolomitization (dolomite), calcitization (calcite), silicification (quartz), and baratization (barite). These alteration styles can be divided into two stages: (1) pre-ore stage of carbonatization that formed re-crystallized Fe-/Mn-bearing dolostone (Fig. 7a), and silicification that generated banded quartz or silicified dolostone (Fig. 7m); and (2) post-ore stage of carbonatization, silicification, and baratization that formed carbonate veinlet or stockwork (dolomite and calcite) (Fig. 7c, 7h–7i, and 7l), quartz and barite vein (Figs. 7f and 7p), respectively. The pre-ore alteration is the result of water/rock

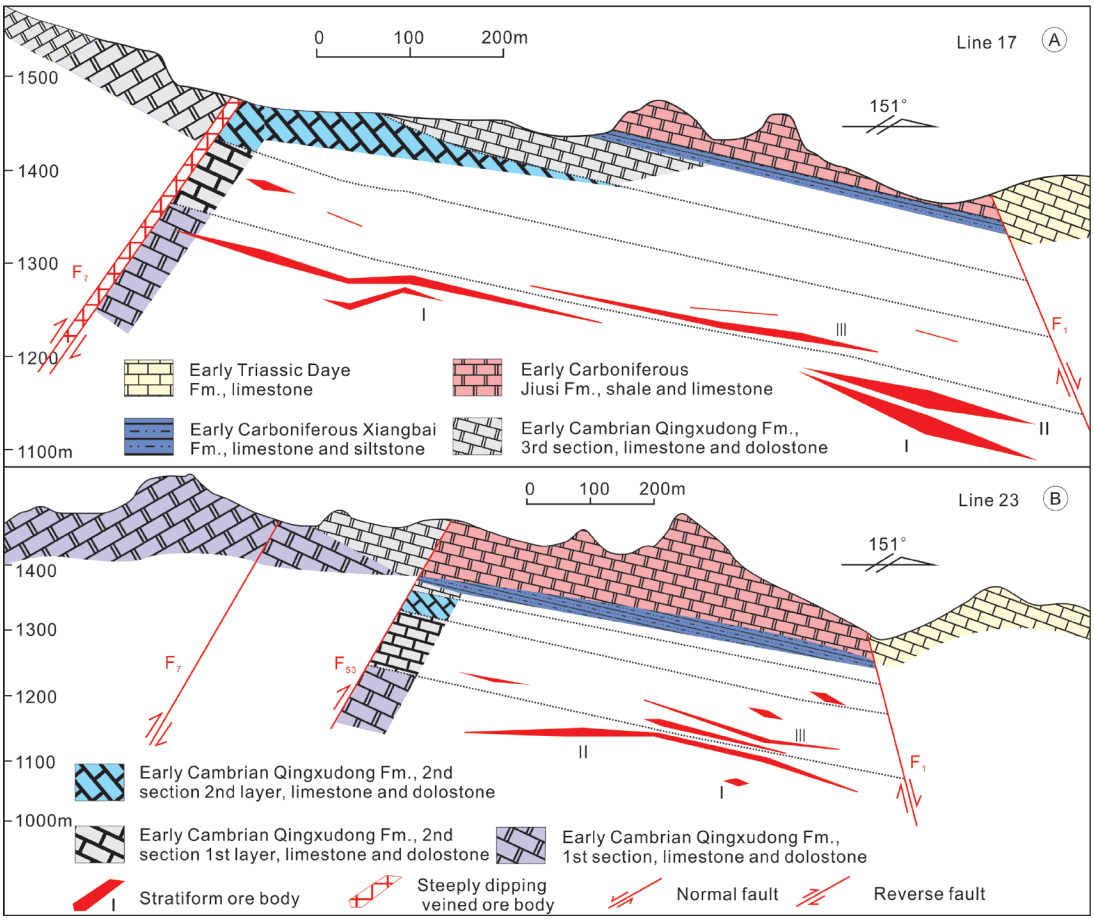

FIGURE 6. (**a**) Cross-section map of No. 17 exploration line (modified from Peng et al. 2016). (**b**) Cross-section map of No. 23 exploration line (modified from Chen et al. 2015a). Strata, lithology, ore body, and fault are shown in both maps. (Color online.)

interaction between hydrothermal fluids and wall rocks, and then resulted in elemental and isotopic exchange. This type of alteration occurs commonly along the structure for fluid migration. The post-ore alteration is the result of late evolution of hydrothermal fluids and is generally close to sulfide ore, and thus can be used as a cue for ore exploration.

SAMPLES AND ANALYTICAL METHODS

Samples

Samples were collected from the exploration engineering of the Nayongzhi Zn-Pb deposit, including drill holes and underground mining tunnels (Figs. 7–8). Seven calcite and 16 sulfide minerals (pyrite and sphalerite) separates were handpicked from 23 sulfide ore samples by micro-drill and binocular microscope. Five limestone whole-rock samples were also collected for C and O isotope analyzing. Five polished thin sections of sulfide ore were used for in situ S and Pb isotope analyzing. In situ S isotopic composition of galena was not determined as no galena standard is available for comparison (Zhang et al. 2014). In addition, in situ Pb isotopic composition of sphalerite and pyrite was not determined, because of the high Hg content of them could significantly affect the quality of the obtained Pb isotopic data (Chen et al. 2014).

Analytical methods

Bulk C-O and S isotope analyses were undertaken using a Finnigan MAT-253 mass spectrometer at the State Key Laboratory of Ore Deposit Geochemistry (SKLODG), Institute of Geochemistry (IG), Chinese Academy Sciences (CAS). Details were described in Appendix[1] B.

In situ S isotope analysis

In situ S isotopic composition was performed by using a CAMECA NanoSIMS 50L at the Key Laboratory of Earth and Planetary Physics, IGGCAS. The measurement was made using three different settings of the Faraday cup (FC) and/or electron multiplier (EM) detector, which meet different requirements for spatial resolution. The effect of EM aging and quasi-simultaneous arrival was corrected before the calibration of instrumental mass fractionation by a standard-sample-standard bracketing method using the standards measured together with the samples. Target spot of the most homogeneous isotopic composition (such as ^{32}S, ^{34}S, and ^{75}As in Fig. 15b) was selected for S isotope analyzing to obtain the credible in situ S isotopic data. International standards included Balmat (pyrite and sphalerite) and CAR 123 (pyrite), and internal standards included PY-1117 (pyrite), CS01 (pyrite), JC-14 (sphalerite), and MY09-12 (sphalerite). The analytical precision calculated from replicate analyses of unknown samples is better than 0.2‰ (1σ). The detail of NanoSIMS in situ S isotope analysis and instrument parameter was described in the reference of Zhang et al. (2014).

In situ Pb isotope analysis

In situ Pb isotopic ratio was determined by using a Nu II MC-ICPMS (Nu Instruments, Wrexham, U.K.) combined with a 266 nm NWR UP Femto femtosecond (fs) laser ablation system (ESI, U.S.A.) at the State Key Laboratory of Continental Dynamics, Northwest University. The surface of the polished thin section was cleaned with milli-Q water (18.2 MΩ·cm). Line scan ablation consisted of background collection for 20 s followed by 50 s of laser ablation for signal collection. Laser ablation parameter is as follows: (1) spot size: 15 μm for galena; (2) 100% output energy: >600 μJ; (3) 100% energy density: 6 J/cm^2; (4) laser frequency: 5–50 Hz; and (5) ablation way: line 3 μm/s. This ensures a strong enough Pb signal for the analyses of sulfide samples. The Tl (20 ppb, NIST SRM 997, $^{205}Tl/^{203}Tl = 2.38890$) and NIST

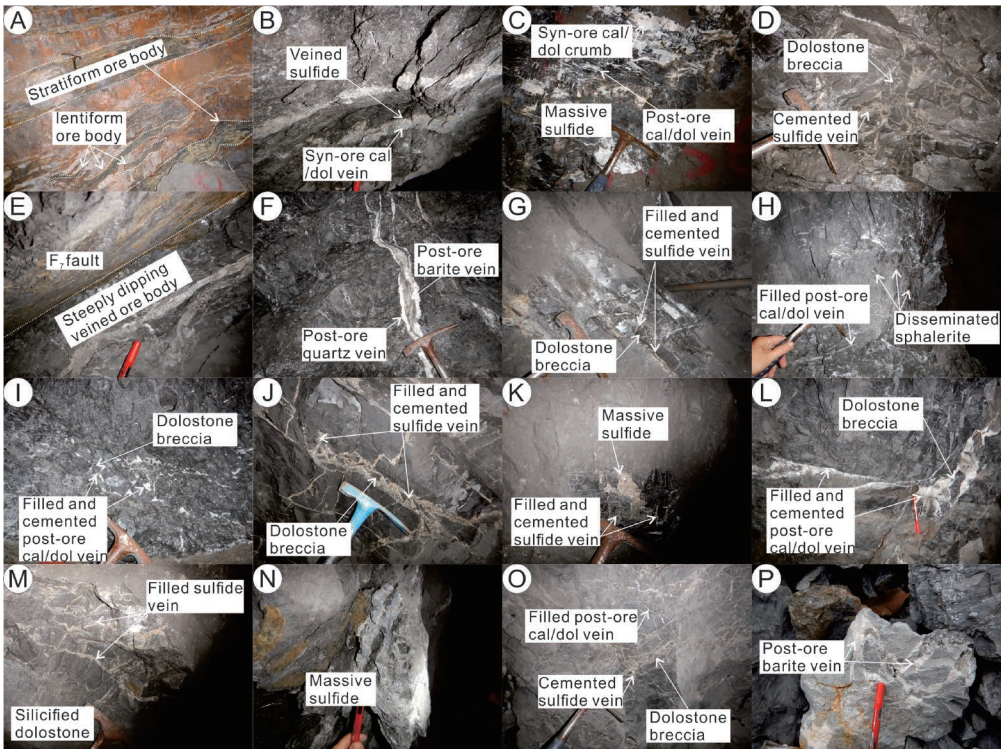

Figure 7. The picture of sulfide ore and post-ore hydrothermal vein, which shows the geometry feature of ore body and aggregate structural feature of hydrothermal minerals. (**a**) Stratiform and lentiform ore bodies. (**b**) Sulfide and carbonate mineral veins. (**c**) Massive sulfide and two phases of calcite/dolomite. (**d**) Sulfide vein cements dolostone breccia. (**e**) Steeply dipping veined ore body occurs along F_7 reverse fault. (**f**) Post-ore quartz and barite vein fills into fracture of wall rocks. (**g**) Sulfide vein fills and cements dolostone breccia. (**h**) Disseminated sphalerite and post-ore calcite/dolomite fills into fracture of wall rocks. (**i**) Post-ore calcite/dolomite vein fills and cements dolostone breccia. (**j**) Sulfide vein cements dolostone breccia. (**k**) Massive sulfide and veined sulfide cements dolostone breccia. (**l**) Post-ore calcite/dolomite vein fills and cements dolostone breccia. (**m**) Sulfide vein fills into fracture of silicified dolostone. (**n**) Massive sulfide. (**o**) Sulfide vine cements dolostone breccia and post-ore calcite/dolomite vein fills into fracture of wall rocks. (**p**) Post-ore barite vein fills into fracture of wall rocks. (Color online.)

SRM 610 glass were served as internal and external standards, respectively. The repeated analyses of NIST SRM 610 glass standard yielded highly reliable and reproducible results during the whole analytical process with mean $^{206}Pb/^{204}Pb$, $^{207}Pb/^{204}Pb$, and $^{208}Pb/^{204}Pb$ ratios of 17.052 ± 0.003, 15.515 ± 0.003, and 36.980 ± 0.007 (1σ, n = 183), respectively. The detail of fs LA-MC-ICPMS in situ Pb isotope analysis and instrument parameter was described in the references of Chen et al. (2014) and Bao et al. (2016).

Analytical results

Carbon and oxygen isotopic composition

Carbon and oxygen isotopic data of limestone whole-rock samples and syn-ore calcite separates are presented in Table 1, and are shown in Figures 11 to 13. Limestone samples have $\delta^{13}C$ and $\delta^{18}O$ values ranging from –1.7 to +1.3‰ and +24.1 to +25.5‰, respectively. Calcite separates have $\delta^{13}C$ values ranging from –4.1 to +0.5‰ and $\delta^{18}O$ values from +12.4 to +14.1‰. The calcite-II separates have higher $\delta^{13}C$ values (–1.9 to +0.5‰) and lower $\delta^{18}O$ values (+12.4 to +13.6‰) than that of calcite-III separate ($\delta^{13}C$ = –4.1‰ and $\delta^{18}O$ = +14.1‰). A marked negative relationship between $\delta^{13}C$ and $\delta^{18}O$ values of all the calcite separates is shown in Figure 11.

Bulk and in situ S isotopic composition

Bulk and in situ S isotopic data are listed in Table 2, and are shown in Figures 14 to 15. Sulfide separates have bulk $\delta^{34}S$ values ranging from +17.17 to +24.79‰, of which pyrite and sphalerite separates have $\delta^{34}S$ values ranging from +18.12 to +22.06‰ and +17.17 to +24.79‰, respectively. In addition, bulk $\delta^{34}S$ values (+22.51 to +24.79‰) of sphalerite-I overlap with those of sphalerite-II ($\delta^{34}S$ = +17.17 to +24.59‰). The NanoSIMS in situ $\delta^{34}S$ values of sulfide crystals range from +11.8 to +33.0‰, of which pyrite and sphalerite crystals have in situ $\delta^{34}S$ values ranging from +15.1 to +27.0‰ and +11.8 to +33.0‰, respectively. As shown in Figure 14c, in situ S isotopic data have a much wider range than bulk S isotopic data. A significant feature of both sphalerite and pyrite crystals is that the in situ $\delta^{34}S$ values decrease from core to rim (sphalerite: decreasing from +33.0 to +11.8‰; pyrite: decreasing from +27.0 to +15.1‰; Fig. 15a).

In situ Pb isotopic ratio

In situ Pb isotopic ratios of galena are presented in Appendix[1] Table 2, and are shown in Figures 16 to 18. Galena crystals have in situ Pb isotopic ratios as follows: $^{206}Pb/^{204}Pb$ = 17.83–17.87, $^{207}Pb/^{204}Pb$ = 15.65–15.67, and $^{208}Pb/^{204}Pb$ = 37.92–38.00 with μ ($^{238}U/^{204}Pb$) values of 9.64–9.67. The galena-I (fine-grained) crystals have $^{206}Pb/^{204}Pb$ ratios of 17.83–17.84, $^{207}Pb/^{204}Pb$ ratios of 15.65–15.67, and $^{208}Pb/^{204}Pb$ ratios of 37.92–37.97, which are slightly lower than those of galena-II crystals (coarse-grained)

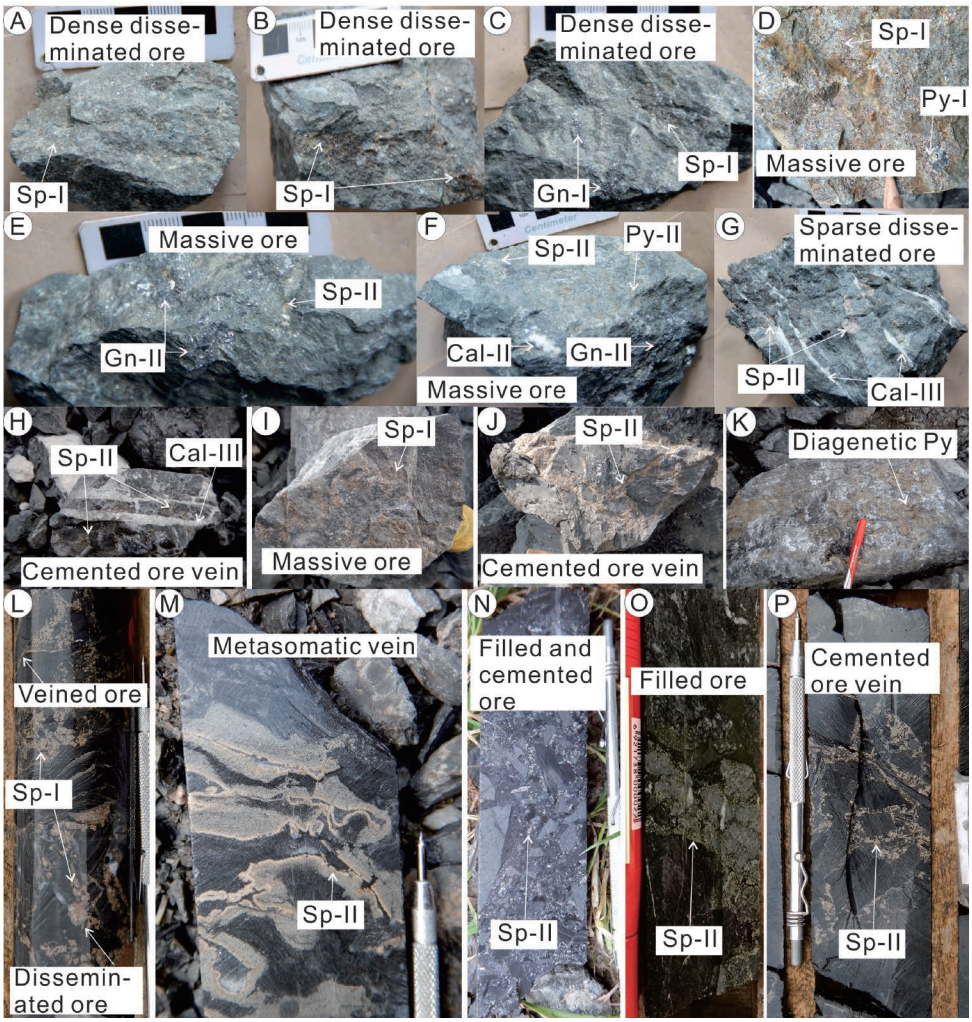

FIGURE 8. The structural feature of sulfide ore in the Nayongzhi deposit. (**a** and **b**) Sphalerite-I occurs as dense disseminated. (**c**) Sphalerite-I occurs as dense disseminated and galena-I presents as sparse disseminated. (**d**) Sphalerite-I and pyrite-I form massive ore. (**e**) Sphalerite-II and galena-II form massive ore. (**f**) Sphalerite-II, galena-II, and pyrite-II form massive ore. (**g**) Sphalerite-II presents as spare disseminated and calcite-III vein fills into fracture of ore. (**h**) Sphalerite-II vein cements dolostone breccia and calcite-III vein fills into fracture of ore. (**i**) Sphalerite-I forms massive ore. (**j**) Sphalerite-II vein cements dolostone breccia. (**k**) Diagenetic pyrite in wall rocks. (**l**) Sphalerite-II presents as disseminated or veined. (**m**) Sphalerite-II replaces wall rocks and forms metasomatic vein. (**n**) Sphalerite-II fills and cements carbonate breccia. (**o**) Sphalerite-II fills into fracture of wall rocks. (**p**) Sphalerite-II cements carbonate breccia. (Color online.)

($^{206}Pb/^{204}Pb$ = 17.84–17.87, $^{207}Pb/^{204}Pb$ = 15.65–15.67, and $^{208}Pb/^{204}Pb$ = 37.93–38.00) (Figs. 17a and 17b).

DISCUSSION

Source of mineralizing elements

Source of CO_2. Carbon and oxygen isotopic compositions of CO_2 of different origins are distinct. For example, mantle-derived CO_2 has $\delta^{13}C$ values ranging from –8 to –4‰ and $\delta^{18}O$ values from +6 to +10‰ (Taylor et al. 1967; Demény et al. 1998), whereas marine carbonate rocks-derived CO_2 has $\delta^{13}C$ = –4 to +4‰ and $\delta^{18}O$ = +20 to +30‰ (Veizer and Hoefs 1976), and the $\delta^{13}C$ and $\delta^{18}O$ values of sedimentary organic matter-derived CO_2 range from –30 to –15‰ and +24 to +30‰, respectively (Hoefs 2009).

Calcite and dolomite are the two main C-bearing hydrothermal minerals in the Nayongzhi sulfide ore (Figs. 6–7). Therefore, H_2CO_3 [present as CO_2 (aqueous)] and HCO_3^- are two key C species in hydrothermal fluids as evidenced by fluid inclusion observation (Zhu et al. 2016). Given that the C isotope fractionation between H_2CO_3 or HCO_3^- (liquid) and CO_2 (gas) is negligible, i.e., $\delta^{13}C_{fluid} \approx \delta^{13}C_{CO_2}$ (Ohmoto 1972), we could obtain the theoretical $\delta^{13}C_{fluid}$ value according to the calculated $\delta^{13}C_{CO_2}$ value.

With an average homogenization temperature of 180 °C (fluid inclusions in quartz-II that formed synchronously with calcite-II; Zhu et al. 2016), the $\delta^{13}C_{CO_2}$ values that range from –4.2 to +0.4‰ were calculated by using the function of $1000\ln\alpha_{(CO_2\text{-calcite})} = -2.4612 + 7.663 \times 10^3/(T + 273.15) - 2.988 \times 10^6/(T + 273.15)^2$ (Bottinga 1968; T = 180 °C). Similarly, the $\delta^{18}O_{H_2O}$ values that vary from +2.3 to +4.0‰ were calculated by using the function of $1000\ln\alpha_{(calcite\text{-}H_2O)} = 2.78 \times 10^6/(T + 273.15)^2 - 3.39$ (O'Neil et al. 1969; T = 180 °C).

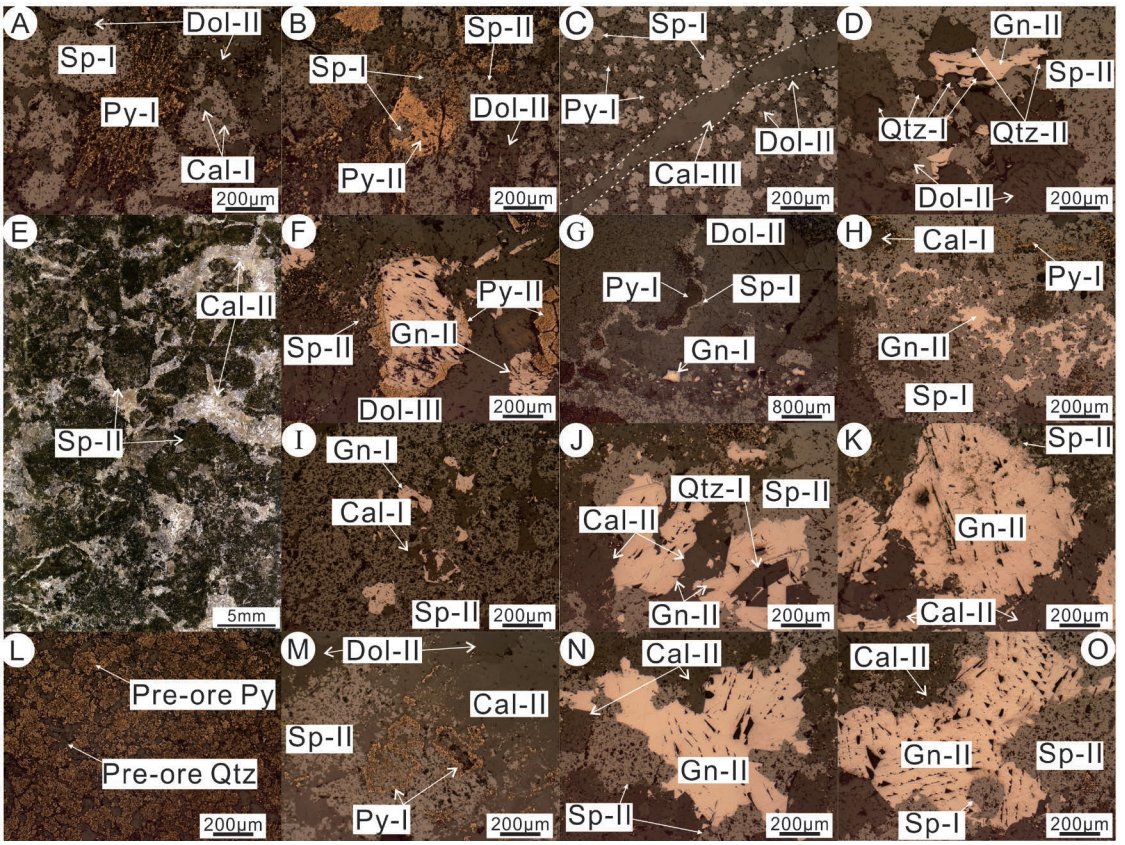

FIGURE 9. The textural feature of hydrothermal minerals in the Nayongzhi deposit under microscope. (**a**) Fine-grained calcite-I (Cal-I) is enclosed by sphalerite-I (Sp-I) that coexists with pyrite-I (Py-I), both of which are cemented by dolomite-II (Dol-II). (**b**) Sp-I is enclosed by Py-II that coexists with Sp-II and Dol-II. (**c**) Sp-I and Py-I are cemented by Dol-II, Cal-III fills into the fracture. (**d**) Quartz-I (Qtz-I) is enclosed by galena-II (Gn-II) that coexists with Sp-II, Dol-II, and Qtz-II. (**e**) Coarse-grained Sp-II coexists with or is cemented by Cal-II. (**f**) Sp-II coexists with Gn-II and Py-II, both of which are cemented by Dol-III. (**g**) Fine-grained Gn-I and veined Py-I and Sp-I are enclosed by Dol-II. (**h**) Fine-grained Py-I and Cal-I are enclosed by Sp-I that are replaced by Gn-II. (**l**) Diagenetic Py is cemented by Qtz. (**m**) Py-I is replaced by Sp-II that coexists with Cal-II. (**n**) Coarse-grained Gn-II coexists with Sp-II and Cal-II. (**p**) Fine-grained Sp-I is enclosed by Gn-II that coexists with Sp-II and Cal-II. (Color online.)

As shown in Figure 11, the proposed $\delta^{13}C_{fluid}$ values (–4.2 to +0.4‰) are higher than those of the mantle and sedimentary organic matter, but are similar to those of both fresh limestone and typical marine carbonate rocks. However, the calculated $\delta^{18}O_{fluid}$ values (+2.3 to +4.0‰) are different from the above three geological reservoirs, but overlap with those of metamorphic water (+2 to +25‰: Hoefs 2009). Therefore, the theoretical $\delta^{13}C_{fluid}$ and $\delta^{18}O_{fluid}$ values suggest that the source of C is the main ^{13}C-enriched limestone, while O is from a mixed source of ^{18}O-depleted metamorphic water and ^{18}O-enriched limestone. As suggested by in situ S and Pb isotopic evidence (Figs. 14–18), the ore-hosting sedimentary rocks and underlying metamorphic rocks are the two principal sources of mineralizing elements and associated fluids for the Nayongzhi deposit (see below).

Mechanism of calcite precipitation. Because the solubility of calcite decreases with increasing of temperature (Zheng 1990; Barnes 1997), cooling of hydrothermal fluids themselves could not result in calcite precipitation. In an open hydrothermal system, the major mechanism that can cause calcite precipitation include fluid mixing, water/rock (W/R) interaction and CO_2 degassing (Zheng 1990; Zheng and Hoefs 1993; Hoefs 2009; Du et al. 2017). The high and uniform C isotopic composition of syn-ore calcite suggests a main limestone source for C (Fig. 11), and so the fluid mixing cannot be the dominant mechanism resulting in calcite precipitation. The W/R interaction can generate a circulating process between dissolution and re-crystallization of local carbonate (Warren 2000). Such a circulating process of carbonate precipitation → dissolution → re-precipitation produced the metastable physical-chemical condition that is requested for giant sulfide mineralization and contributed to calcite precipitation. Furthermore, using C and O isotope fractionation factors and equations (O'Neil et al. 1969; Zheng and Hoefs 1993), we simulated the C and O isotopic evolution curves of calcite precipitated by the interaction between supposed metamorphic fluids ($\delta^{13}C_{fluid}$ = –2‰, $\delta^{18}O_{fluid}$ = +6‰) and carbonate rocks (Fig. 12). The simulation result suggests that our C and O isotopic data match well with the evolution curve of HCO_3^- as the dominant C species (Fig. 12; Zheng and Hoefs 1993). Similarly, the C and O isotopic compositions of calcite precipitated by CO_2 degassing (with 0.1, 0.2, 0.3 and 0.4 mole fraction of total C and O; $\delta^{13}C_{fluid}$ = –2‰, $\delta^{18}O_{fluid}$ = +6‰) were simulated (Figs. 13a and 13b). The result shows that our C and O isotopic data still match well with the evolution curve of HCO_3^- as

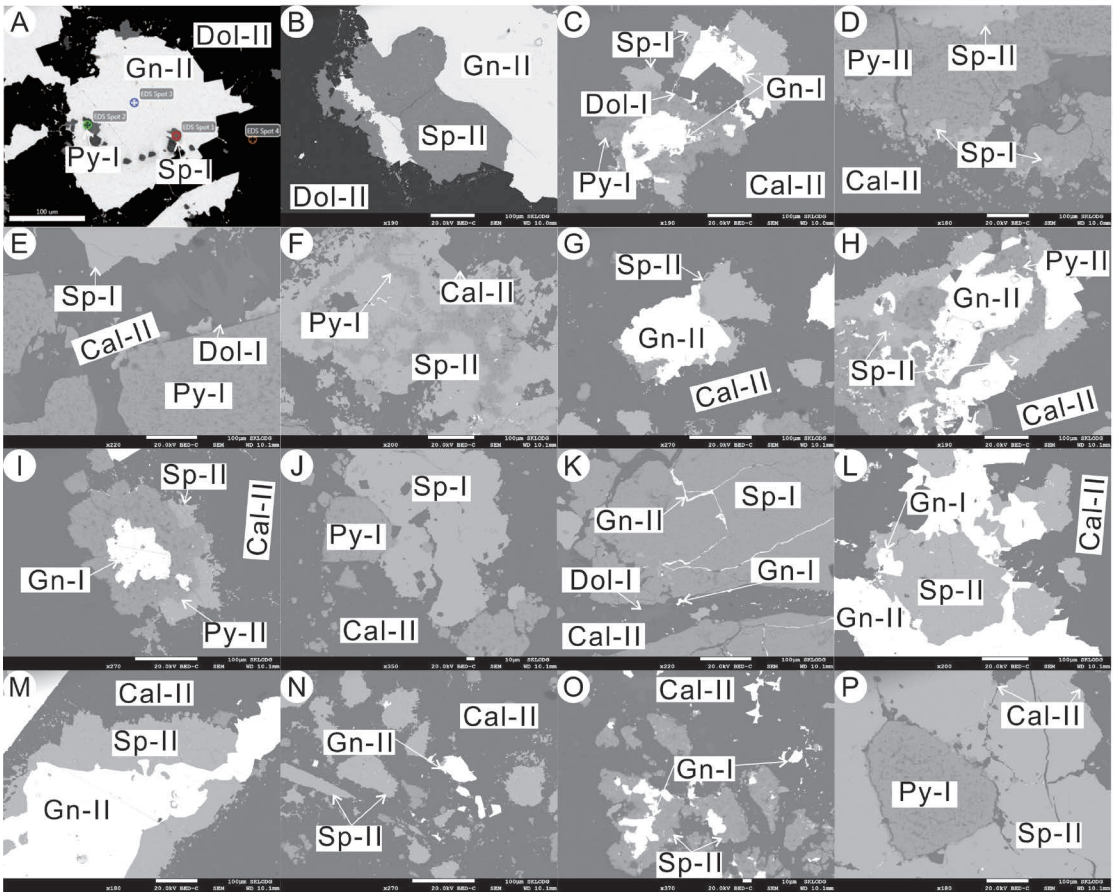

FIGURE 10. The textural feature of hydrothermal minerals in the Nayongzhi deposit under scanning electron microscope (SEM). (**a**) Fine-grained sphalerite-I (Sp-I) and pyrite-I (Py-I) are enclosed by galena-II (Gn-II) that is cemented by dolomite-II (Dol-II). (**b**) Sp-II coexists with Gn-II and Dol-II. (**c**) Paragenetic Sp-I, Gn-I, Py-I, and Dol-I are enclosed by calcite-II (Cal-II). (**d**) Fine-grained Sp-I is enclosed by Py-II that coexists with Sp-II, Cal-II fills into the fracture. (**e**) Dol-I is enclosed by Cal-II, which fills into the boundary of Sp-I and Py-I. (**f**) Sp-II replaces Py-I and coexists with Cal-II. (**g**) Paragenetic Sp-II and Gn-II are enclosed by Cal-II. (**h**) Paragenetic Sp-II, Py-II, and Gn-II are enclosed by Cal-II. (**i**) Py-II encloses Gn-I and coexists with Sp-II, both of which are enclosed by Cal-II. (**j**) Paragenetic Sp-I and Py-I are enclosed by Cal-II. (**k**) Fine-grained Gn-I and Dol-I are enclosed by Cal-II; Gn-II and Cal-II fill into the fracture of sphalerite-I. (**l**) Sp-II encloses fine granular Gn-I and coexists with Gn-II and Cal-II. (**m**) Paragenetic Sp-II, Gn-II, and Cal-II. (**n**) Cal-II cements Sp-II and Gn-II. (**o**) Call-II fills and cements Sp-II that contains Gn-I. (**p**) Sp-II encloses granular Py-I and coexists with Cal-II. (Color online.)

the dominant C species (Fig. 13b). We thus propose that both the W/R interaction and CO_2 degassing are the main mechanisms for calcite precipitation in the Nayongzhi deposit.

Source of S, formation mechanism, and isotope fractionation

Source of S. The fact that both in situ S isotopic data ($\delta^{34}S$ = +11.8 to +33.0‰) and the bulk ones ($\delta^{34}S$ = +17.17 to +24.79‰) (Table 2) reflect the enrichment of ^{34}S in hydrothermal fluids, a typical characteristic of marine sulfate-derived S. In additional, it has been well documented that $\delta^{34}S_{barite} > \delta^{34}S_{fluid} > \delta^{34}S_{sulfide}$ if the hydrothermal minerals contain barite (Ohmoto 1972; Ohmoto et al. 1990). Thus, the $\delta^{34}S_{fluid}$ value should be higher than the minimum or average $\delta^{34}S_{sulfide}$ value determined by in situ and bulk analyses (Figs. 14–15) as recorded by the paragenetic association of barite in post-ore phase (Appendix[1] Table 1; Peng et al. 2016), i.e., $\delta^{34}S_{fluid}$ > +11.8 or +17.17‰ (minimum in situ and bulk $\delta^{34}S_{sulfide}$ values, respectively) or +21.7‰ (mean value of all measured data). Such S isotopic signatures differ from mantle-derived S (0 ± 3‰: Chaussidon et al. 1989), but overlap with those of the sulfate-bearing (barite/gypsum) evaporates within Cambrian to Triassic marine sedimentary strata in the studied region (Fig. 14b; $\delta^{34}S$ = +22 to +28‰: Jin 2008; Zhou et al. 2013a) and the Ediacaran to Cambrian seawater (Figs. 14a–14b; $\delta^{34}S$ = +25 to +35‰: Claypool et al. 1980; Seal 2006). As $\Delta^{34}S_{sulfate\text{-}sulfide}$ can be high up to +15‰ in the process of thermochemical sulfate reduction (Ohmoto et al. 1990; Machel et al. 1995; Worden et al. 1995; Ohmoto and Goldhaber 1997), so the theoretical $\delta^{34}S_{sulfide}$ value could down to +7‰ or +10‰, if the reduced S was completely derived from evaporates or seawater. The theoretically predicted $\delta^{34}S_{sulfide}$ values sourced from both of the above two reservoirs can match well with the observed $\delta^{34}S$ values (> +11.8‰; Fig. 14c). This suggests multiple S reservoirs for S^{2-} in the studied deposit. Previous studies showed that the S in the nearby carbonate-hosted Zn-Pb deposits, such as Shaojiwan (hosts in permian), Tianqiao, Qingshan, and Shanshulin (host in carboniferous) (Figs. 2, 14a,

TABLE 1. C-O isotopic compositions of calcite and limestone in the Nayongzhi deposit

No.	Mineral/ Rock	$\delta^{13}C_{PDB}$ (‰)	$\delta^{18}O_{PDB}$ (‰)	$\delta^{18}O_{SMOW}$ (‰)	$\delta^{13}C_{CO_2}$ (‰)[a]	$\delta^{18}O_{H_2O}$ (‰)[b]
H06-6	Calcite-III	−4.1	−16.2	+14.1	−4.2	+4.0
H06-17	Calcite-II	−0.7	−17.9	+12.4	−0.8	+2.3
1290F-4	Calcite-II	−1.9	−16.7	+13.6	−2.0	+3.5
1390Cal	Calcite-II	−0.2	−17.3	+13.0	−0.3	+2.9
1390JP-4	Calcite-II	−1.4	−16.8	+13.6	−1.5	+3.5
1390JP-6	Calcite-II	−1.1	−17.5	+12.9	−1.2	+2.8
1390JP-7	Calcite-II	+0.5	−17.6	+12.7	+0.4	+2.6
YH1220-1	Limestone	+0.2	−6.5	+24.2		
YH1220-2	Limestone	+0.6	−6.2	+24.5		
YH1220-3	Limestone	+0.8	−5.2	+25.5		
YH1220-4	Limestone	+1.3	−6.6	+24.1		
YH1220-5	Limestone	−1.7	−5.7	+25.0		

Notes: $\delta^{18}O_{SMOW} = 1.03086 \times \delta^{18}O_{PDB} + 30.86$ (Friedman and O'Neil 1977); the error is ±0.2‰ (2σ) for $\delta^{13}C$ and ±1‰ (2σ) for $\delta^{18}O$. T = 180 °C, based on temperature analysis of fluid inclusion in quartz-II (Zhu et al. 2016).

[a] $1000\ln\alpha_{(CO_2\text{-calcite})} = -2.4612 + 7.663 \times 10^3/(T + 273.15) - 2.988 \times 10^6/(T + 273.15)^2$ (Bottinga 1968).

[b] $1000\ln\alpha_{(calcite\text{-}H_2O)} = 2.78 \times 10^6/(T + 273.15)^2 - 3.39$ (O'Neil et al. 1969).

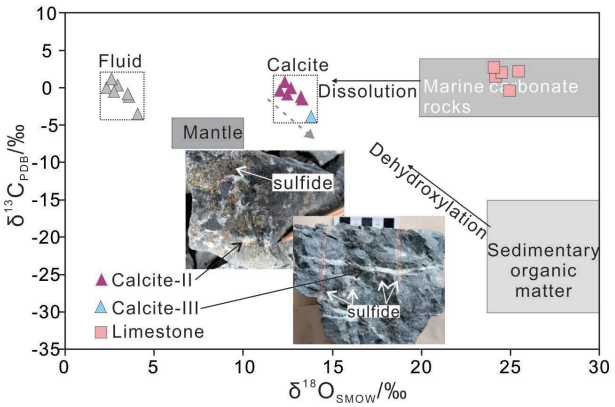

FIGURE 11. Plot of $\delta^{13}C$ vs. $\delta^{18}O$ values. C-O isotopic data for mantle, marine carbonate rocks and sedimentary organic matter are sourced from Taylor et al. (1967), Demény et al. (1998), Veizer and Hoefs (1976), and Hoefs (2009). (Color online.)

and 14b), is also derived from multiple S reservoirs (Zhou et al. 2013a, 2014b; Li et al. 2015).

Formation mechanism of reduced S. Two mechanisms, including bacterial sulfate reduction (BSR) and thermochemical sulfate reduction (TSR), have been employed to explain the formation of S^{2-} from SO_4^{2-} (Seal 2006; Basuki et al. 2008; Zhou et al. 2014a). These two reduction processes are temperature-dependent. BSR occurs at a relatively low T (<110 °C: Jørgenson et al. 1992; Basuki et al. 2008). The homogenization temperature of fluid inclusions in quartz (113–232 °C; Zhu et al. 2016) is too high for bacteria to survive. So BSR played an insignificant role in the formation of S^{2-}. TSR occurs at a relatively high T (>100–140 °C: Machel et al. 1995; Worden et al. 1995) and can produce a large amount of S^{2-}, with relatively stable $\delta^{34}S$ values (Ohmoto et al. 1990; Seal 2006). Moreover, the mixed process of hot and cold ore-forming fluids could form S^{2-} from SO_4^{2-} by TSR through the reactions of $SO_4^{2-} + 2C = S^{2-} + 2CO_2$, $SO_4^{2-} + CH_4 = H_2S + CO_3^{2-} + H_2O$, or $SO_4^{2-} + 2CH_2O = H_2S + 2HCO_3^-$ (Worden et al. 1995; Leach et al. 2005). We thus propose that the TSR has played a key role in the formation of S^{2-} in the Nayongzhi deposit.

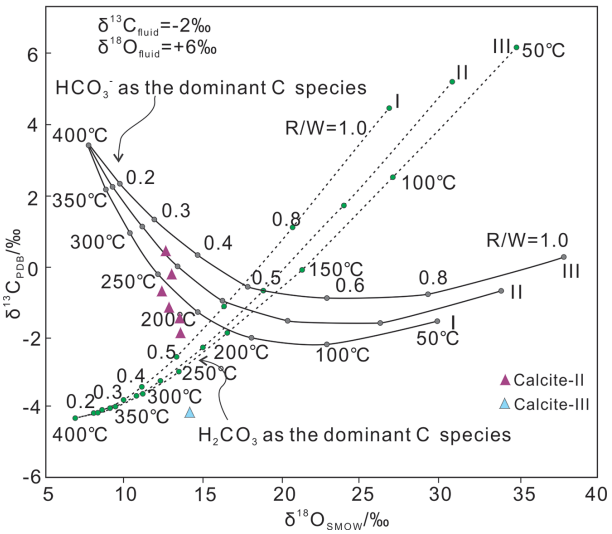

FIGURE 12. Plot of $\delta^{13}C$ vs. $\delta^{18}O$ for the calcite precipitated by W/R interaction with variation of R/W ratio and temperature (400–50 °C) for either HCO_3^- or H_2CO_3 as the dominant dissolved C species (Zheng and Hoefs 1993). Initial metamorphic fluids: $\delta^{13}C = -2‰$, $\delta^{18}O = +6‰$. $\Delta = \delta^i_{rock} - \delta^f_{rock}$; (**I**) $\Delta^{13}C = +0.2‰$, $\Delta^{18}O = +2‰$; (**II**) $\Delta^{13}C = +1‰$, $\Delta^{18}O = +6‰$; (**III**) $\Delta^{13}C = +2‰$, $\Delta^{18}O = +10‰$. (Color online.)

S isotope fractionation. The similarity of bulk S isotopic composition between pyrite ($\delta^{34}S$ = +18.12 to +22.06‰) and sphalerite ($\delta^{34}S$ = +17.17 to +24.79‰) precipitated at different ore-forming stages (Appendix[1] Table 1; Fig. 14c) indicates that the bulk S isotopic data could not reflect the real S isotope fractionation. The imparity of in situ $\delta^{34}S$ values between pyrite (+15.1 to +27.0‰) and sphalerite (+11.8 to +33.0‰) crystals suggests that in situ determined S isotopes can reflect the nature of fractionation involved in mineralization. As shown in Figure 15a, rims of pyrite crystal have $\delta^{34}S$ values (+15.1 to +15.3‰) higher than those of rims of paragenetic sphalerite crystal ($\delta^{34}S$ = +11.8 to +11.9‰). Such S isotopic signatures suggest that S isotope fractionation between pyrite and paragenetic sphalerite has reached thermodynamic equilibrium (Ohmoto et al. 1990; Seal 2006). We thus propose an equilibrium S isotope fractionation between paragenetic sulfide minerals, at least locally.

In addition, the in situ S isotopic ratios decrease from the core to rim of both pyrite and sphalerite crystals (Fig. 15a), which can be explained by: (1) variation of physical-chemical condition (T, pH, f_{O_2}, etc.) in single S reservoir (Seal 2006); (2) mixture of multiple S reservoirs (Ohmoto et al. 1990); or (3) dynamic fractionation of S isotopes (Hoefs 2009). Previous studies suggested that the change of physical-chemical condition can cause significant variation of S isotopes in hydrothermal system (Seal 2006; Hoefs 2009). However, the circulating process of carbonate dissolution → re-precipitation can provide a metastable environment for giant mineralization (see above), so the variation of physical-chemical condition is indistinctive, and thus plays an insignificant role in the decreasing $\delta^{34}S$ values from core to rim of sulfide crystals. The mixed process of the heavy S isotope-enriched fluid and the ^{34}S-depleted fluid can cause significant variation of S isotopes (Seal 2006). Both bulk and in

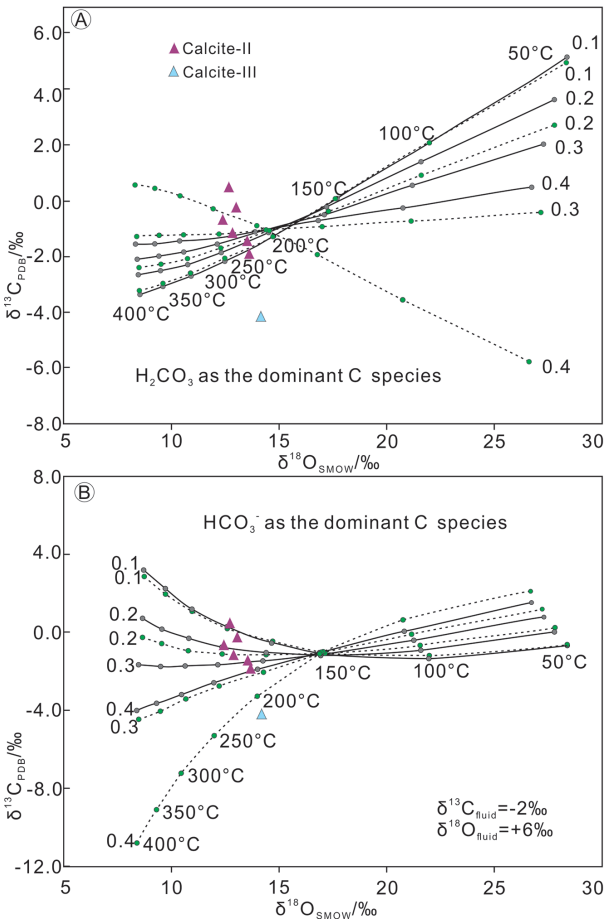

Figure 13. Plots of $\delta^{13}C$ vs. $\delta^{18}O$ for calcite precipitated by CO_2 degassing with H_2CO_3 (**a**) or HCO_3^- (**b**) as the dominant dissolved C species. The batch (solid line) and Rayleigh (dashed line) degassing-precipitation models change with temperature (400–50 °C) and mole fraction of C in the degassed CO_2 (0.1 to 0.4) (after Zheng 1990). The $\delta^{13}C$ and $\delta^{18}O$ values of the initial ore-forming fluids were taken as –2‰ and +6‰, respectively. (Color online.)

Table 2. Bulk S and in situ S isotopic compositions of sulfide minerals in the Nayongzhi deposit

No.	Sample	Stage	$\delta^{34}S_{CDT}$ (‰)	Note
2015HT-2-0	Pyrite	Stage I	+22.06	Whole-mineral
2015JP-1-1	Pyrite	Stage I	+18.12	
2015HT-2-1	Yellow sphalerite	Stage II	+21.04	
2015HT-2-2	Brown-yellow sphalerite	Stage II	+22.42	
2015HT-2-3	Brown sphalerite	Stage I	+22.51	
2015HT-1-1	Yellow sphalerite	Stage II	+24.59	
2015HT-1-2	Brown-yellow sphalerite	Stage II	+23.60	
2015HT-1-3	Brown-red sphalerite	Stage I	+24.73	
2015HT-1-3	Brown-red sphalerite	Stage I	+24.79	
2015HT-5-1	Yellow sphalerite	Stage II	+23.57	
2015HT-5-2	Brown-yellow sphalerite	Stage II	+23.64	
2015HT-5-3	Brown-red sphalerite	Stage I	+23.27	
2015HT-4-1	Yellow sphalerite	Stage II	+17.17	
2015HT-4-2	Brown-yellow sphalerite	Stage II	+21.95	
2015HT-4-3	Brown sphalerite	Stage I	+24.17	
2015HT-4-3	Brown sphalerite	Stage I	+24.20	
W-1	Sphalerite-I	Core	+33.0	In situ
W-2	Sphalerite-I	Core	+32.5	
W-3	Sphalerite-I	Rim	+12.0	
W-4	Sphalerite-I	Rim	+12.3	
W-5	Sphalerite-I	Rim	+11.9	
W-6	Sphalerite-I	Rim	+11.8	
W-7	Pyrite-I	Rim	+15.1	
W-8	Pyrite-I	Rim	+15.3	
W-9	Pyrite-I	Rim	+24.4	
W-10	Pyrite-I	Rim	+24.5	
W-11	Pyrite-I	Core	+26.1	
W-12	Pyrite-I	Core	+27.0	

Note: The error is ±0.2‰ (2σ) for bulk $\delta^{34}S$ and ±0.2‰ (1σ) for in situ $\delta^{34}S$.

situ S isotopic data in this study suggests multiple S reservoirs for S^{2-} in the Nayongzhi deposit, so the observed decrease of S isotopes from core to rim of sulfide crystals (Fig. 15a) may be the result of a mixture of multiple S reservoirs. Alternatively, the rapid precipitation of sulfide minerals can cause a strong Rayleigh fractionation of S isotopes during the process of fluid mixing. As a consequence of the dynamic fractionation, ^{34}S is expected to be more enriched in the core of sulfide crystals than their rim (Fig. 15a).

Source of ore-forming metal. Because of extremely low contents of U and Th in sulfide minerals (especially galena), time-integrated effect of U and Th on radiogenic Pb isotopes in sulfides is negligible (Carr et al. 1995; Muchez et al. 2005; Pass et al. 2014; Zhou et al. 2014b). Therefore, the Pb isotopic ratios of galena from the Nayongzhi deposit can represent those of hydrothermal fluids. The narrow range of in situ Pb isotopic data suggests a single source or else a well-mixed source of Pb (Appendix[1] Table 2; Figs. 16a and 16b). In the plot of $^{207}Pb/^{204}Pb$ vs. $^{206}Pb/^{204}Pb$ (Fig. 16a), all the Pb isotopic data plot in the field that overlaps with the Pb evolution curve of the upper crust contributed to the orogeny and the field of modern lower crust (Zartman and Doe 1981). Similarly, in the $^{208}Pb/^{204}Pb$ vs. $^{206}Pb/^{204}Pb$ diagram (Fig. 16b), all the Pb isotopic data also plot into the field of modern lower crust (Zartman and Doe 1981). This suggests that the source of Pb is the deep continental crust (Zartman and Doe 1981). Again, the μ values ($^{238}U/^{204}Pb$ = 9.64–9.67) of the galena are slightly higher than that of the mean value of the continental crust (μ = 9.58), also indicating a deep-seated crustal source for Pb (Carr et al. 1995).

As shown in Figure 16a, at a given $^{207}Pb/^{204}Pb$ ratio, the galena displays significantly lower $^{206}Pb/^{204}Pb$ ratios than those of the Permian Emeishan flood basalts, and Ediacaran carbonate rocks. Such Pb isotopic signatures rule out the main contribution of Pb metal from mantle-derived magmatic rocks and ore-hosting sedimentary rocks. On the contrary, in situ Pb isotopic ratios of the galena are similar to those of the Proterozoic metamorphic rocks (Fig. 16a). This further suggests a continental crustal origin for Pb in hydrothermal fluids and the basement rocks provided the majority of Pb metal.

The in situ Pb isotopic ratios gradually increase from galena-I (fine-grained) to galena-II (coarse-grained) in both $^{207}Pb/^{204}Pb$ vs. $^{206}Pb/^{204}Pb$ (Fig. 17a) and $^{208}Pb/^{204}Pb$ vs. $^{206}Pb/^{204}Pb$ diagrams (Fig. 17b). There are two possibilities: (1) U and Th contents of galena-II are relatively higher than those of galena-I or (2) high radiogenic Pb-enriched source provides more Pb for galena-II than galena-I. Trace elements determined by LA-ICPMS show that there is no significant difference of both U and Th contents between two generations of galena (Ye et al. 2011 and unpublished data). Furthermore, Pb isotopic data of galena-I overlap with those of galena-II in the diagram of $^{208}Pb/^{206}Pb$ vs. $^{207}Pb/^{206}Pb$

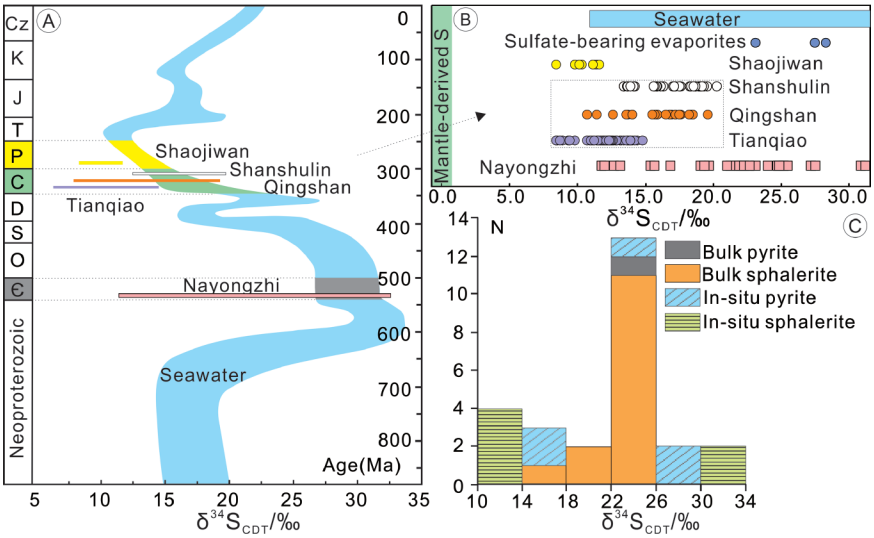

FIGURE 14. (**a**) S isotopic composition for seawater sulfate, and the Nayongzhi and nearby Zn-Pb deposits. (**b**) S isotopic composition for the Nayongzhi deposit and a brief comparison with the nearby Zn-Pb deposits, sulfate-bearing evaporites, seawater, and mantle-derived S. (**c**) Histogram of bulk and in situ S isotopic composition for the Nayongzhi deposit. S isotopic data for the nearby Zn-Pb deposits and evaporites are taken from Jin (2008), Zhou et al. (2013a, 2014b), and Li et al. (2015), for the mantle-derived S are taken from Chaussidon et al. (1989), for the seawater are taken from Claypool et al. (1980) and Seal (2006). (Color online.)

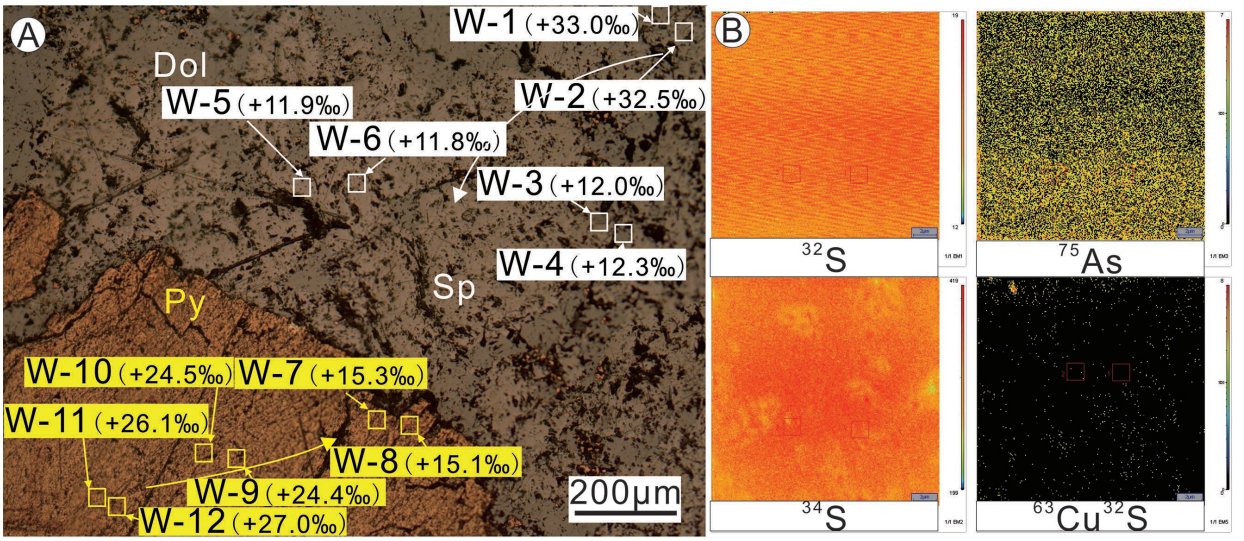

FIGURE 15. (**a**) In situ $\delta^{34}S$ value in sphalerite and paragenetic pyrite crystals from core to rim. (**b**) The best target selected for in situ S isotope analysis that has homogeneous isotopic composition (such as ^{32}S, ^{34}S, ^{75}As, and $^{63}Cu^{32}S$). (Color online.)

(Fig. 18), suggesting that both of them have the same contents of U and Th. On the contrary, in both $^{207}Pb/^{204}Pb$ vs. $^{206}Pb/^{204}Pb$ (Fig. 17a), $^{208}Pb/^{204}Pb$ vs. $^{206}Pb/^{204}Pb$ (Fig. 17b), and $^{208}Pb/^{206}Pb$ vs. $^{207}Pb/^{206}Pb$ diagrams (Fig. 18), the Pb isotopic compositions of two generations of galena form two distinct evolution curves. This implies that the high radiogenic Pb-enriched source (most likely the ore-hosting sedimentary rocks) provides more Pb for the ore-forming fluids at the late phase than the early phase, and thus slightly changes the evolution curve of Pb isotopes.

Timing of mineralization

The occurrence of ore body (Fig. 6) and sulfide ore (Figs. 7–8), and the evidence of mineralogy (Figs. 9–10) and isotope geochemistry (Figs. 11–18) show that the Nayongzhi deposit belongs to epigenetic type. This means that the formation of the Nayongzhi deposit should occur after the ore-hosting late Ediacaran and early Cambrian strata. In addition, the Nayongzhi deposit is located at the northern margin of the Triassic Youjiang Basin and is structurally controlled by the Wuzhishan fold-fault system (Figs. 2–4), all of which were active during the Yanshanian Orogeny (Chen et

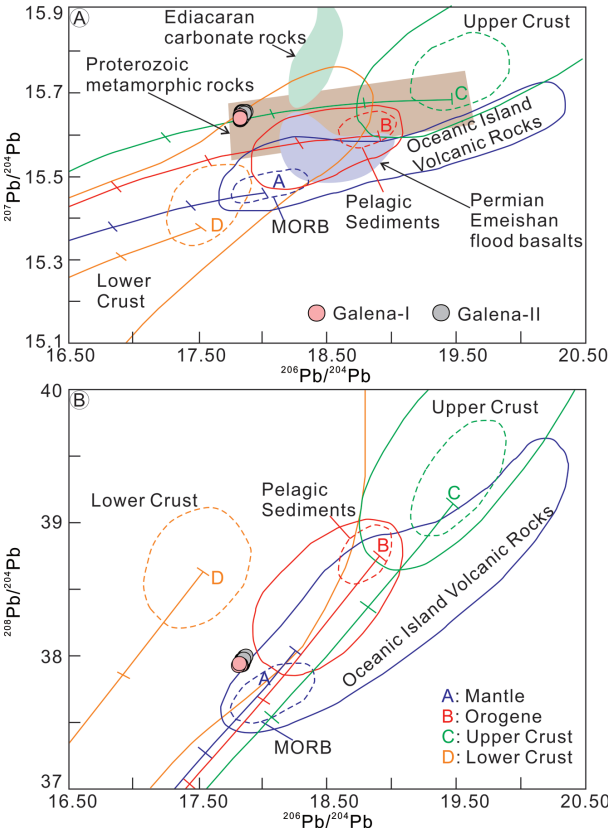

FIGURE 16. Plots of $^{207}Pb/^{204}Pb$ vs. $^{206}Pb/^{204}Pb$ (**a**) and $^{208}Pb/^{204}Pb$ vs. $^{206}Pb/^{204}Pb$ (**b**) that present a brief comparison of the modern MORB, Pelagic sediment, Oceanic island volcanic rocks, upper crust and lower crust Pb (Zartman and Doe 1981), and whole-rock of Ediacaran carbonate rocks, Permian Emeishan basalts and Proterozoic metamorphic rocks (Li et al. 2007; Yan et al. 2007; Zhou et al. 2013a, 2014a). Solid lines enclose 80% of all data points for each field, and dashed lines enclose probable average values. Mantle (**a**), Orogeny (**b**), Upper crust contributed to the orogeny (**c**), and lower crust contributed to the orogeny (**d**). (Color online.)

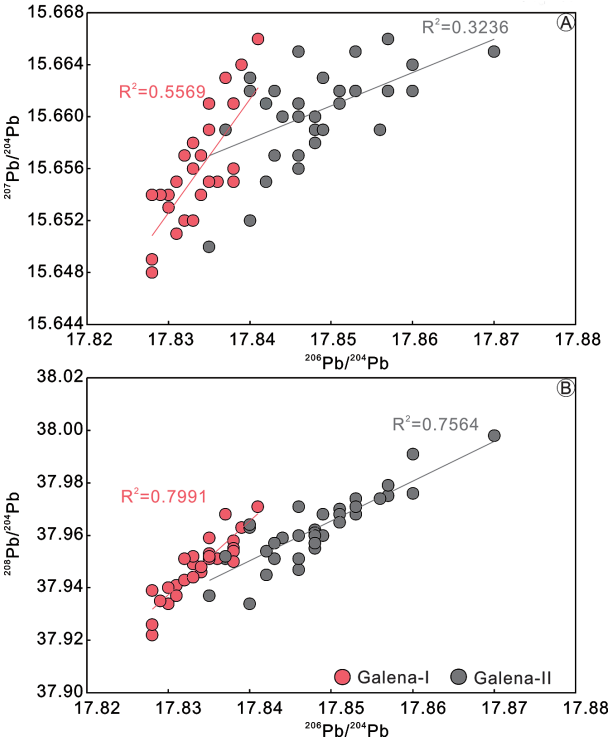

FIGURE 17. Plots of $^{207}Pb/^{204}Pb$ vs. $^{206}Pb/^{204}Pb$ (**a**) and $^{208}Pb/^{204}Pb$ vs. $^{206}Pb/^{204}Pb$ that reveal the variation in Pb isotopes from the early phase galena-I to the late phase galena-II. (Color online.)

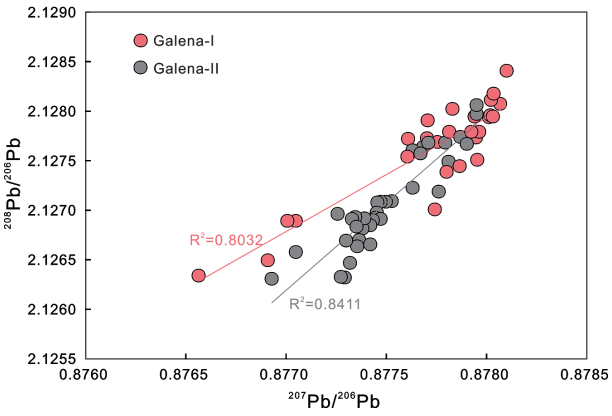

FIGURE 18. Diagram of $^{208}Pb/^{206}Pb$ vs. $^{207}Pb/^{206}Pb$ that shows the relationship and evolution of two generations of galena. (Color online.)

al. 2015a). Such an ore-controlling structure feature suggests that the Nayongzhi deposit was most likely formed in the Yanshanian period. Moreover, isotope geochronology studies suggest that the ages of carbonate-hosted Zn-Pb deposits in the SYG province are 226–165 Ma (Mao et al. 2012; Zhou et al. 2013a; Zhang et al. 2015). Therefore, we propose that the Nayongzhi deposit formed in the early Yanshanian (late Triassic) and related to the evolution of the Triassic Youjiang Basin, and it was most likely to be the product of basin-orogeny coupling.

IMPLICATIONS

Ore genesis type

The ore body of the Nayongzhi deposit occurs as in stratiform or lentiform (Figs. 6a, 6b, and 7a) shape, which has led some researchers to classify it as a SEDEX-type or sedimentation reworking type of deposit (Chen et al. 2015a; Jin et al. 2015). In fact, with the exception of the stratiform or lentiform Zn-Pb ore body, there are steeply dipping veined aspects that are also developed (Figs. 6a and 7e). Furthermore, the ore-hosting rocks are late Ediacaran and early Cambria carbonate rocks, which differ from the siliciclastic rocks that host sulfide ores of the Sedimentary Exhalative-type (Leach et al. 2005, 2010). The newly obtained bulk C-O and S isotopes, and in situ S and Pb isotopes, together with ore deposit geology and mineralogy, suggest an epigenetic origin for the Nayongzhi deposit.

Extensive studies have suggested that the carbonate-hosted Zn-Pb deposits of the Sichuan-Yunnan-Guizhou are characterized by: (1) a close spatial association with the Emeishan mafic magmatism (Fig. 1b); (2) high grade, i.e., > 10 wt% Zn + Pb, and

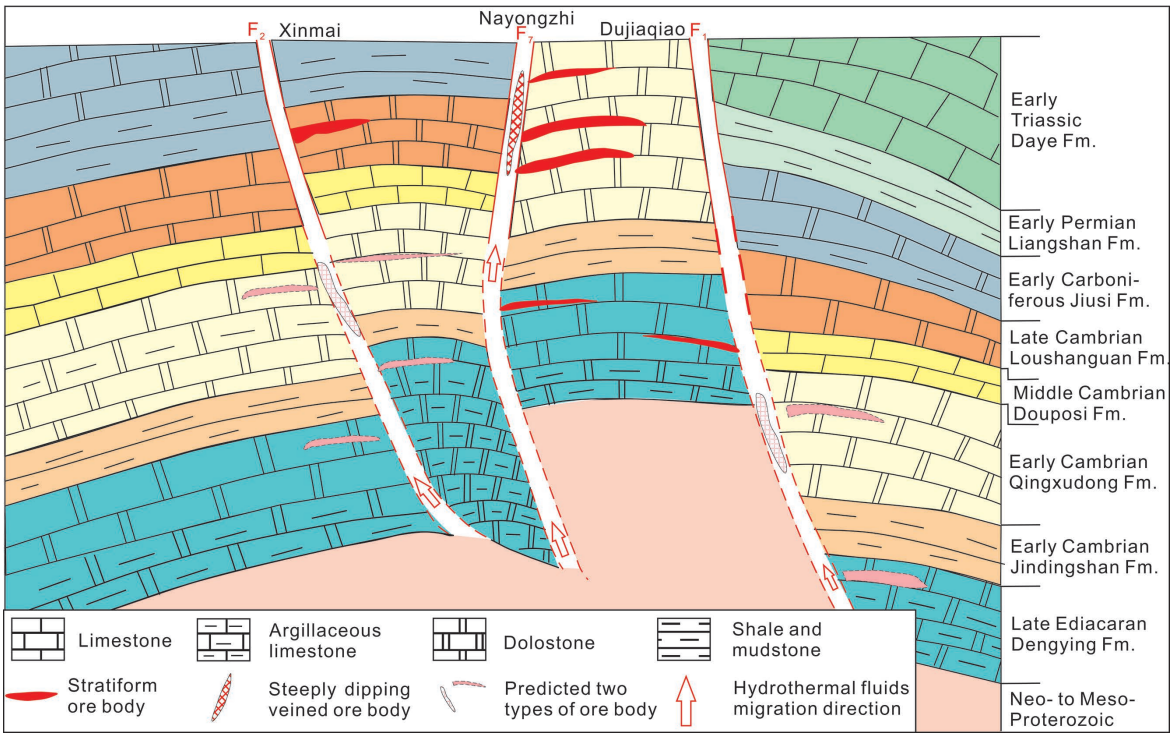

FIGURE 19. An integrated working and ore exploration model of the carbonate-hosted Zn-Pb deposits in the Wuzhishan anticline area. (Color online.)

high concentrations of Ag, Cu, Cd, Ge, and Ga (Ye et al. 2011; Zhou et al. 2013a; Zhu et al. 2017); (3) ore-forming fluids with low-medium temperature (120–280 °C) and low salinity (2–10 wt% NaCl equiv.) (Li et al. 2007; Zhou et al. 2014a; Zhu et al. 2016); and (4) a mixed metal source of overlying basalts, ore-hosting sedimentary rocks, and underlying metamorphic rocks (Huang et al. 2010; Zhou et al. 2014b; Li et al. 2015, 2016). However, the Nayongzhi deposit is distinct from the nearby Zn-Pb deposits (Appendix[1] Table 3) in that: (1) the ore body has no direct genetic association with igneous activity (Fig. 4); (2) sulfide ores have low ore grade, with an average of 8–10 wt% Zn + Pb; (3) ore-forming fluids exhibit low temperature (113–232 °C) and moderate salinity (10–15 wt% NaCl equiv.) (Zhu et al. 2016); (4) basement-derived metals are dominant in hydrothermal fluids (Fig. 16a); and (5) carbonate solution collapse breccias are well developed (Figs. 7–8). These mineralized features of the Nayongzhi deposit can be compared to those of typical MVT deposits (Leach et al. 2005, 2010). So we interpret the Nayongzhi deposit to be an epigenetic Mississippi Valley-type deposit.

Ore formation process: A new model

We propose a new working model to explain the Zn-Pb mineralization in the Wuzhishan anticline area (Fig. 19) as follows: The basement-derived metal-bearing metamorphic fluids (as suggested by C-O and Pb isotopes; Figs. 12–13 and 16–18) were driven upward along the regional Yadu-Ziyun fault (Figs. 2–3) by the late Indosinian Orogeny (226–205 Ma) and coeval with the formation of the Triassic Youjiang Basin (Zhou et al. 2013a; Chen et al. 2015b; Zhang et al. 2015). The fluids were released into secondary structural units (such as the Wuzhishan anticline; Figs. 2–3) when the tectonic regime shifted from compression to extension in the early Yanshanian (205–165 Ma) (Qiu et al. 2016). These fluids were trapped into the platform carbonate sequences, where evaporitic salt and sedimentary organic-bearing units are well developed (Fig. 19). This process resulted in the formation of S^{2-} from SO_4^{2-} by thermochemical sulfate reduction and the extraction of mineralizing elements from the ore-hosting strata via the water/rock interaction (as evidenced by C-O, S, and Pb isotopes; Figs. 12–18). The rapid sulfide precipitation caused by mixing multiple S reservoirs with associated fluids resulted in significant fractionation of S isotopes (Figs. 14a–14c and 15a). During the ore formation process, local carbonate acted as a buffer through repeated dissolution and re-precipitation, providing a metastable metallogenic environment for massive sulfide mineralization. According to our new model, some potential and buried ore bodies may be found in the future (Fig. 19).

These results imply that the extensional setting (Youjiang Basin) facilitated the excretion of hydrothermal fluids; the fold structure (Wuzhishan anticline) was beneficial to the entrapment of fluids; the carbonate platform sequences supplied the source of S and organic reducers; and the various fluids then mixed as the carbonate buffer caused rapid and continued precipitation of sulfide minerals, all of which are crucial for the formation and exploration of Mississippi Valley-type deposits in general.

ACKNOWLEDGMENTS

We thank Lin Ye and Rui-Zhong Hu (IGCAS), and David Leach (U.S. Geological Survey) for fruitful discussions. Fang-Zhen Teng (Associate Editor), Ben-Xun Su, and anonymous reviewers are also thanked for their constructive suggestions and comments. This research was financially supported by the Key Project of National

Natural Science Foundation of China (41430315), the National Basic Research Program of China (2014CB440905), the Visiting Scholar Project of China Scholarship Council to Jia-Xi Zhou (201604910455), and ARC Future Fellowship (No. FT140100826) to Xuan-Ce Wang.

REFERENCES CITED

Bai, J., Huang, Z., Zhu, D., Yan, Z., and Zhou, J. (2013) Isotopic compositions of sulfur in the Jinshachang lead-zinc deposit, Yunnan, China, and its implication on the formation of sulfur-bearing minerals. Acta Geologica Sinica (English Edition), 87, 1355–1369.

Bao, Z., Yuan, W., Yuan, H., Liu, X., Chen, K., and Zong, C. (2016) Non-matrix-matched determination of lead isotope ratios in ancient bronze artifacts by femtosecond laser ablation multi-collector inductively coupled plasma mass spectrometry. International Journal of Mass Spectrometry, 402, 12–19.

Barnes, H.L. (1997) Geochemistry of Hydrothermal Ore Deposits. Wiley

Barker, S.L., Hickey, K.A., Cline, J.S., Dipple, G.M., Kilburn, M.R., Vaughan, J.R., and Longo, A.A. (2009) Uncloaking invisible gold: Use of nanoSIMS to evaluate gold, trace elements, and sulfur isotopes in pyrite from Carlin-type gold deposits. Economic Geology, 104, 897–904.

Basuki, N.I., Taylor, B.E., and Spooner, E.T.C. (2008) Sulfur isotope evidence for thermo-chemical reduction of dissolved sulfate in Mississippi valley type zinc-lead mineralization, Bongara area, northern Peru. Economic Geology, 103, 183–799.

Bottinga, Y. (1968) Calculation of fractionation factors for carbon and oxygen isotopic exchange in the system calcite-carbon dioxide-water. The Journal of Physical Chemistry, 72, 800–808.

Carr, G.R., Dean, J.A., Suppel, D.W., and Heithersay, P.S. (1995) Precise lead isotope fingerprinting of hydrothermal activity associated with Ordovician to Carboniferous metallogenic events in the Lachlan fold belt of New South Wales. Economic Geology, 90, 1467–1505.

Carter, A., Roques, D., Bristow, C., and Kinny, P. (2001) Understanding Mesozoic accretion in Southeast Asia: significance of Triassic thermotectonism (Indosinian orogeny) in Vietnam. Geology, 29, 211–214.

Chaussidon, M., Albarède, F., and Sheppard, S.M.F. (1989) Sulphur isotope variations in the mantle from ion microprobe analyses of micro-sulphide inclusions. Earth and Planetary Science Letters, 92, 144–156.

Chen, K.Y., Yuan, H.L., Bao, Z.A., Zong, C.L., and Dai, M.N. (2014) Precise and accurate in situ determination of lead isotope ratios in NIST, USGS, MPI-DING and CGSG glass reference materials using femtosecond laser ablation MC-ICP-MS. Geostandards and Geoanalytical Research, 38, 5–21.

Chen, G.Y., Wang, L., Fan, Y.M., and Zheng, W. (2015a) Ore-search prospect of the deep subsurface in the Wuzhishan Pb-Zn ore field, Guizhou province. Geology and Exploration, 51, 859–869 (in Chinese with English abstract).

Chen, M., Zhang, Z., Santosh, M., Dang, Y., and Zhang, W. (2015b) The Carlin-type gold deposits of the "golden triangle" of SW China: Pb and S isotopic constraints for the ore genesis. Journal of Asian Earth Sciences, 103, 115–128.

Claypool, G.E., Holser, W.T., Kaplan, I.R., Sakai, H., and Zak, I. (1980) The age curves of sulfur and oxygen isotopes in marine sulfate and their mutual interpretation. Chemical Geology, 28, 199–260.

Demény, A., Ahijado, A., Casillas, R., and Vennemann, T.W. (1998) Crustal contamination and fluid/rock interaction in the carbonatites of Fuerteventura (Canary Islands, Spain): A C, O, H isotope study. Lithos, 44, 101–115.

Du, L.J., Li, B., Huang, Z.L., Zhou, J.X., Zou, G.F., and Yan, Z.F. (2017) Carbon-oxygen isotopic geochemistry of the Yangla Cu skarn deposit, SW China: Implications for the source and evolution of hydrothermal fluids. Ore Geology Reviews, 88, 809–821.

Friedman, I., and O'Neil, J.R. (1977) Compilation of stable isotope fractionation factors of geochemical interest. Data of Geochemistry, U.S. Geological Survey Professional Paper, 440-KK, 1–12.

Gao, S., Yang, J., Zhou, L., Li, M., Hu, Z.C., Guo, J.L., Yuan, H.L., Gong, H.J., Xiao, G.Q., and Wei, J.Q. (2011) Age and growth of the Archean Kongling terrain, South China, with emphasis on 3.3 Ga granitoid gneisses. American Journal of Sciences, 311, 153–182.

Gustafson, L.B., and Williams, N. (1981) Sediment-hosted stratiform deposits of copper, lead and zinc. Economic Geology, 75, 139–178.

Heijlen, W., Muchez, P., Banks, D., Schneider, J., Kucha, H., and Keppens, E. (2003) Carbonate-hosted Zn-Pb deposits in Upper Silesia, Poland: Origin and evolution of mineralizing fluids and constraints on genetic models. Economic Geology, 98, 911–932.

Hoefs, J. (2009) Stable Isotope Geochemistry (sixth edition). Springer-Verlag, doi: 10.1007/978-3-540-70708-0.

Hu, R.Z., and Zhou, M.F. (2012) Multiple Mesozoic mineralization events in South China-an introduction to the thematic issue. Mineralium Deposita, 47, 579–588.

Hu, R., Fu, S., Huang, Y., Zhou, M., Fu, S., Zhao, C., Wang, Y., Bi, X., and Xiao, J. (2017) The giant South China Mesozoic low-temperature metallogenic domain: Reviews and a new geodynamic model. Journal of Asian Earth Sciences, 137, 9–34.

Huang, Z., Li, X., Zhou, M., Li, W., and Jin, Z. (2010) REE and C-O isotopic geochemistry of calcites from the word-class Huize Pb-Zn deposits, Yunnan, China: Implication for the ore genesis. Acta Geologica Sinica (English edition), 84, 597–613.

Ikehata, K., Notsu, K., and Hirata, T. (2008) In situ determination of Cu isotope ratios in copper-rich materials by NIR femtosecond LA-MC-ICPMS. Journal of Analytical Atomic Spectrometry, 23, 1003–1008.

Jian, P., Li, D.Y., Kröner, A., Zhang, Q., Wang, Y.Z., Sun, X.M., and Zhang, W. (2009) Devonian to Permian plate tectonic cycle of the Paleo-Tethys Orogen in southwest China (II): Insights from zircon ages of ophiolites, arc/back-arc assemblages and within-plate igneous rocks and generation of the Emeishan CFB province. Lithos, 113, 767–784.

Jin, Z.G. (2008) The ore-control factors, ore-forming regularity and ore forecasting of Pb-Zn deposits in NW Guizhou province. Engine Industry Press, Beijing, pp. 1–105 (in Chinese).

Jin, C.H., Li, K., Huang, L., Zhang, Y., and Shen, Z.W. (2015) Characteristics of sulfur and lead isotope composition and metallogenic material source of the Nayongzhi Pb-Zn deposit, northwestern Guizhou province. Journal of Mineralogy and Petrology, 35, 81–88 (in Chinese with English abstract).

Jin, Z.G., Zhou, J.X., Huang, Z.L., Luo, K., Gao, J.G., Peng, S., Wang, B., and Chen, X.L. (2016) Ore genesis of the Nayongzhi Pb-Zn deposit, Puding city, Guizhou Province, China: Evidences from S and in situ Pb isotopes. Acta Petrologica Sinica, 32, 3441–3455.

Jørgenson, B.B., Isaksen, M.F., and Jannasch, H.W. (1992) Bacterial sulfate reduction above 100°C in deep sea hydrothermal vent sediments. Science, 258, 1756–1757.

Leach, D.L., Bradley, D.C., Huston, D., Pisarevsky, S.A., Taylor, R.D., and Gardoll, S.J. (2010) Sediment-hosted lead-zinc deposits in Earth history. Economic Geology, 105, 593–625.

Leach, D.L., Sangster, D., Kelley, K.D., Large, R.R., Garven, G., Allen, C., Gutzmer, J., and Walters, S. (2005) Sediment-hosted lead-zinc deposits: A global perspective. Economic Geology, 100th Anniversary, 561–607.

Li, W.B., Huang, Z.L., and Yin, M.D. (2007) Dating of the giant Huize Zn-Pb ore field of Yunnan province, southwest China: Constraints from the Sm-Nd system in hydrothermal calcite. Resource Geology, 57, 90–97.

Li, B., Zhou, J.X., Huang, Z.L., Yan, Z.F., Bao, G.P., and Sun, H.R. (2015) Geological, rare earth elemental and isotopic constraints on the origin of the Banbanqiao Zn-Pb deposit, southwest China. Journal of Asian Earth Sciences, 111, 100–112.

Li, B., Zhou, J., Li, Y., Chen, A., and Wang, R. (2016) Geology and isotope geochemistry of the Yinchanggou-Qiluogou Pb-Zn deposit, Sichuan Province, Southwest China. Acta Geologica Sinica (English Edition), 90, 1768–1779.

Lin, Z.Y., Wang, D.H., and Zhang, C.Q. (2010) Rb-Sr isotopic age of sphalerite from the Paoma lead-zinc deposit in Sichuan Province and its implications. Geology of China, 37, 488–196 (in Chinese with English abstract).

Liu, H.C., and Lin, W.D. (1999) Study on the law of Pb-Zn-Ag ore deposit in northeast Yunnan, China. Kunming, Yunnan University Press, pp. 1–468 (in Chinese).

Liu, Y., Hu, Z., Gao, S., Günther, D., Xu, J., Gao, C., and Chen, H. (2008) In situ analysis of major and trace elements of anhydrous minerals by LA-ICP-MS without applying an internal standard. Chemical Geology, 257, 34–43.

Machel, H.G., Krouse, H.R., and Sassen, R. (1995) Products and distinguishing criteria of bacterial and thermo-chemical sulfate reduction. Applied Geochemistry, 10, 373–389.

Mao, J.W., Zhou, Z.H., Feng, C.Y., Wang, Y.T., Zhang, C.Q., Peng, H.J., and Miao, Y. (2012) A preliminary study of the Triassic large-scale mineralization in China and its geodynamic setting. Geology of China, 39, 1437–1471 (in Chinese with English abstract).

Muchez, P., Heijlen, W., Banks, D., Blundell, D., Boni, M., and Grandia, F. (2005) Extensional tectonics and the timing and formation of basin-hosted deposits in Europe. Ore Geology Reviews, 27, 241–267.

Ohmoto, H., and Goldhaber, M.B. (1997) Sulfur and carbon isotopes. In H.L. Barnes, Ed., Geochemistry of Hydrothermal Ore Deposits, 3rd ed., pp. 517–611. Wiley.

Ohmoto, H., Kaiser, C.J., and Geer, K.A. (1990) Systematic of sulfur isotopes in recent marine sediments and ancient sediment-hosted base metal deposits In H.K Herbert and S.E. Ho, Eds., Stable Isotopes and Fluid Processes in Mineralisation. University of Western Australia, 23, 70–120.

Ohmoto, H. (1972) Systematics of sulfur and carbon isotopes in hydrothermal ore deposits. Economic Geology, 67, 551–579.

O'Neil, J.R., Clayton, R.N., and Mayeda, T.K. (1969) Oxygen isotope fractionation in divalent metal carbonates. Journal of Chemical Physics, 51, 5547–5558.

Pass, H.E., Cookem, D.R., Davidson, G., Maas, R., Dipple, G., Rees, C., Ferreira, L., Taylor, C., and Deyell, C.L. (2014) Isotope geochemistry of the northeast zone, Mount Polley alkalic Cu-Au-Ag porphyry deposit, British Columbia: A case for carbonate assimilation. Economic Geology, 109, 859–890.

Peevler, J., Fayek, M., Misra, K.C., and Riciputi, L.R. (2003) Sulfur isotope microanalysis of sphalerite by SIMS: constraints on the genesis of Mississippi valley-type mineralization, from the Mascot-Jefferson City district, East Tennessee. Journal of Geochemical Exploration, 80, 277–296.

Peng, S., Jin, Z.G., Lin, G.S., Zhu, Y.Q., and Wang, B (2016) Analysis of ore-controlling factors and metallogenic model of Wuzhishan Pb-Zn deposit, Guizhou: A case study of Nayongzhi deposit. Mineral Exploration, 7, 463–470 (in Chinese with English abstract).

Qiu, L., Tang, S.L., Wang, Q., Yang, W.X., Tang, X.L., and Wang, J.B. (2016) Mesozoic geology of southwestern China: Indosinian foreland overthrusting

and subsequent deformation. Journal of Asian Earth Sciences, 122, 91–105.
Qiu, Y.M., Gao, S., McNaughton, N.J., Groves, D.I., and Ling, W.L. (2000) First evidence of >3.2 Ga continental crust in the Yangtze craton of south China and its implications for Archean crustal evolution and Phanerozoic tectonics. Geology, 28, 11–14.
Reid, A., Wilson, C.J.L., Shun, L., Pearson, N., and Belousova, E. (2007) Mesozoic plutons of the Yidun Arc, SW China: U-Pb geochronology and Hf isotopic signature. Ore Geology Reviews, 31, 88–106.
Seal, I.R. (2006) Sulfur isotope geochemistry of sulfide minerals. Reviews in Mineralogy and Geochemistry, 61, 633–677.
Steinhoefel, G., Horn, I., and von Blanckenburg, F. (2009) Micro-scale tracing of Fe and Si isotope signatures in banded iron formation using femtosecond laser ablation. Geochimica et Cosmochimica Acta, 73, 5343–5360.
Taylor, H.P., Frechen, J., and Degens, E.T. (1967) Oxygen and carbon isotope studies of carbonatites from the Laacher See District, West Germany and the Alnö District, Sweden. Geochimica et Cosmochimica Acta, 31, 407–430.
Tu, G.Z. (1984) Geochemistry of Strata-bound Ore Deposits in China (Volumes I). Science Press, Beijing, pp. 13–69 (in Chinese with English abstract).
Veizer, J., and Hoefs, J. (1976) The nature of O^{18}/O^{16} and C^{13}/C^{12} secular trends in sedimentary carbonate rocks. Geochimica et Cosmochimica Acta, 40, 1387–1395.
Warren, J. (2000) Dolomite: Occurrence, evolution and economically important associations. Earth-Science Review, 52, 1–81.
Wang, C.M., Deng, J., Carranza, E.J.M., and Lei, X.R. (2014) Nature, diversity and temporal-spatial distributions of sediment-hosted Pb-Zn deposit in China. Ore Geology Reviews, 56, 327–351.
Wei, A.Y., Xue, C.D., Xiang, K., Li, J., Liao, C., and Akhter, Q.J. (2015) The ore-forming process of the Maoping Pb-Zn deposit, northeastern Yunnan, China: Constraints from cathodoluminescence (CL) petrography of hydrothermal dolomite. Ore Geology Reviews, 70, 562–577.
Wilkinson, J.J., Stoffell, B., Wilkinson, C.C., Jeffries, T.E., and Appold, M.S. (2009) Anomalously metal-rich fluids form hydrothermal ore deposits. Science, 323, 764–767.
Wong, W.H. (1927) Crustal movements and igneous activities in eastern China since Mesozoic time. Bulletin of the Geological Association of China, 6, 9–37.
Worden, R.H., Smalley, P.C., and Oxtoby, N.H. (1995) Gas souring by the thermo chemical sulfate reduction at 140°C. AAPG Bulletin, 79, 854–863.
Xie, J.R. (1963) Introduction of the Chinese Ore Deposits. Scientific Books Publishing House, Beijing, pp. 1–71 (in Chinese).
Xu, Y., Huang, Z., Zhu, D., and Luo, T. (2014) Origin of hydrothermal deposits related to the Emeishan magmatism. Ore Geology Reviews, 63, 1–8.
Yan, D.P., Zhou, M.F., Song, H.L., Wang, X.W., and Malpas, J. (2003) Origin and tectonic significance of a Mesozoic multilayer overthrust system within the Yangtze Block (South China). Tectonophysics, 361, 239–254.
Yan, Z.F., Huang, Z.L., Xu, C., Chen, M., and Zhang, Z.L. (2007) Signatures of the source for the Emeishan flood basalts in the Ertan area: Pb isotope evidence. Chinese Journal of Geochemistry, 26, 207–213.
Ye, L., Cook, N.J., Ciobanu, C.L., Liu, Y.P., Zhang, Q., Liu, T.G., Gao, W., Yang, Y.L., and Danyushevsky, L. (2011) Trace and minor elements in sphalerite from base metal deposits in South China: a LA–ICPMS study. Ore Geology Reviews, 39, 188–217.
Yuan, H.L., Yin, C., Liu, X., Chen, K.Y., Bao, Z.A., Zong, C.L., Dai, M.N., Lai, S.C., Wang, R., and Jiang, S.Y. (2015) High precision in-situ Pb isotopic analysis of sulfide minerals by femtosecond laser ablation multi-collector inductively coupled plasma mass spectrometry. Science China Earth Science, 58, 1713–1721.
Zartman, R.E., and Doe, B.R. (1981) Plumbotectonics—the model. Tectonophysics, 75, 135–162.
Zaw, K., Peters, S.G., Cromie, P., Burrett, C., and Hou, Z.Q. (2007) Nature, diversity of deposit types and metallogenic relations of South China. Ore Geology Reviews, 31, 3–47.
Zhang, J., Lin, Y., Yang, W., Shen, W., Hao, J., Hu, S., and Cao, M. (2014) Improved precision and spatial resolution of sulfur isotope analysis using NanoSIMS. Journal of Analytical Atomic Spectrometry, 29, 1934–1943.
Zhang, C., Wu, Y., Hou, L., and Mao, J. (2015) Geodynamic setting of mineralization of Mississippi Valley-type deposits in world-class Sichuan-Yunnan-Guizhou Zn-Pb triangle, southwest China: Implications from age-dating studies in the past decade and the Sm-Nd age of the Jinshachang deposit. Journal of Asian Earth Sciences, 103, 103–114.
Zheng, Y.F. (1990) Carbon-oxygen isotopic covariation in hydrothermal calcite during degassing of CO_2. Mineralium Deposita, 25, 246–250.
Zheng, Y.F., and Hoefs, J. (1993) Carbon and oxygen isotopic covariations in hydrothermal calcites. Mineralium Deposita, 28, 79–89.
Zheng, M.H., and Wang, X.C. (1991) Genesis of the Daliangzi Pb-Zn deposit in Sichuan, China. Economic Geology, 86, 831–846.
Zhou, C.X., Wei, C.S., and Guo, J.Y. (2001) The source of metals in the Qilingchang Pb-Zn deposit, Northeastern Yunnan, China: Pb-Sr isotope constraints. Economic Geology, 96, 583–598.
Zhou, M.F., Yan, D.P., Kennedy, A.K., Li, Y.Q., and Ding, J. (2002) SHRIMP zircon geochronological and geochemical evidence for Neo-Proterozoic arc-related magmatism along the western margin of the Yangtze Block, South China. Earth and Planetary Science Letters, 196, 1–67.
Zhou, J., Huang, Z., Zhou, M., Li, X., and Jin, Z. (2013a) Constraints of C-O-S-Pb isotope compositions and Rb-Sr isotopic age on the origin of the Tianqiao carbonate-hosted Pb-Zn deposit, SW China. Ore Geology Reviews, 53, 77–92.
Zhou, J., Huang, Z., and Yan, Z. (2013b) The origin of the Maozu carbonate-hosted Pb-Zn deposit, southwest China: Constrained by C-O-S-Pb isotopic compositions and Sm-Nd isotopic age. Journal of Asian Earth Sciences, 73, 39–47.
Zhou, J.X., Huang, Z.L., Zhou, M.F., Zhu, X.K., and Muchez, P. (2014a) Zinc, sulfur and lead isotopic variations in carbonate-hosted Pb-Zn sulfide deposits, southwest China. Ore Geology Reviews, 58, 41–54.
Zhou, J.X., Huang, Z.L., Lv, Z.C., Zhu, X.K., Gao, J.G., and Mirnejad, H. (2014b) Geology, isotope geochemistry and ore genesis of the Shanshulin carbonate-hosted Pb-Zn deposit, southwest China. Ore Geology Reviews, 63, 209–225.
Zhou, M.F., Zhao, X.F., Chen, W.T., Li, X.C., Wang, W., Yan, D.Y., and Qiu, H.N. (2014c) Proterozoic Fe-Cu metallogeny and supercontinental cycles of the southwestern Yangtze Block, southern China and northern Vietnam. Earth-Science Review, 139, 59–82.
Zhou, J.X., Bai, J.H., Huang, Z.L., Zhu, D., Yan, Z.F., and Lv, Z.C. (2015) Geology, isotope geochemistry and geochronology of the Jinshachang carbonate-hosted Pb-Zn deposit, southwest China. Journal of Asian Earth Sciences, 98, 272–284.
Zhu, L.Y., Su, W.C., Shen, N.P., Dong, S.D., Cai, J.L., Zhang, Z.W., Zhao, H., and Xie, P. (2016) Fluid inclusion and sulfur isotopic studies of lead-zinc deposits, northwestern Guizhou, China. Acta Petrologica Sinica, 32, 3431–3440 (in Chinese with English abstract).
Zhu, C.W., Wen, H.J., Zhang, Y.X., Fu, S.H., Fan, H.F., and Cloquet, C. (2017) Cadmium isotope fractionation in the Fule Mississippi Valley-type deposit, Southwest China. Mineralium Deposita, 52, 675–686.

Manuscript received July 10, 2017
Manuscript accepted August 30, 2017
Manuscript handled by Fang-Zhen Teng

Endnote:

[1]Deposit item AM-18-16238, Appendix Tables and Appendix Material A and B. Deposit items are free to all readers and found on the MSA web site, via the specific issue's Table of Contents (go to http://www.minsocam.org/MSA/AmMin/TOC/2018/Jan2018_data/Jan2018_data.html).